CHARACTERIZATION OF POROUS MATERIALS USING MOLECULAR THEORY AND SIMULATION

Christian M. Lastoskie

Department of Chemical Engineering, Michigan State University, East Lansing, Michigan 48824

Keith E. Gubbins

Department of Chemical Engineering, North Carolina State University, Raleigh, North Carolina 27695

I. Introduction

Characterization of the pore structure of amorphous adsorbents and disordered porous catalysts remains an important chemical engineering research problem. Pore structure characterization requires both an effective experimental probe of the porous solid and an appropriate theoretical or numerical model to interpret the experimental measurement. Gas adsorption porosimetry [1] is the principal experimental technique used to probe the structure of the porous material, although various experimental alternatives have been proposed including immersion calorimetry [2–4], positron

0065-2377/01 $35.00

annihilation [5], transmission electron microscopy [6, 7], and small-angle X-ray [7, 8] or neutron [9] scattering. Consequently, most pore structure analysis methods attempt to address the question of how properly to interpret gas sorption uptake measurements on porous solids to obtain an accurate picture of the porous material structure.

Two approaches may be taken in devising a pore structure model to apply to experimental measurements. In one approach, a *disordered model microstructure* is assembled that explicitly incorporates the amorphous nature of the adsorbent into the theoretical model. For example, an activated carbon might be represented as a randomly oriented assemblage of graphitic disks of uniform size and composition [10]. In the other approach, a *simple geometric model* of the adsorbent pore structure is utilized, and the amorphous character of the porous solid is implicitly represented through structure distribution functions. In this case, the pore volume of the aforementioned activated carbon might be modeled as an array of slit-shaped pores with a distribution of slit widths [11]. Not surprisingly, the substitution of a simplified geometric model for the actual structure of a disordered adsorbent invokes major assumptions regarding pore shape, connectivity, and chemical composition. At best, these assumptions will introduce a degree of uncertainty into the characterization results, and in some instances, the simple pore geometries may be altogether unsuitable for describing the adsorbent structure. However, analysis methods that are based upon simple geometric models generally lend themselves to convenient and efficient numerical solution, whereas fitting the structure parameters of a model disordered adsorbent can be quite difficult and computationally intensive to carry out. For this reason, a great majority of the thermodynamic models for interpreting experimental gas adsorption isotherms are based upon simple geometric representations of pore structure that, for the most part, do not directly incorporate the effects of pore shape variation, pore connectivity, or chemical heterogeneity.

The thermodynamic models used to represent adsorption in either the disordered or the simple geometric description of the pore volume may be classified into four categories, presented in decreasing order of computational intensiveness.

1. *Molecular simulation* calculations of the theoretical adsorption isotherm for a model pore structure under the experimental conditions: This involves principally either grand canonical Monte Carlo (GCMC) [12] or Gibbs ensemble Monte Carlo (GEMC) [13] simulation of adsorption in regular pore geometries but also includes reverse Monte Carlo (RMC) [14] simulation methods for the interpretation of pore morphologies from scattering data.

2. *Statistical thermodynamic theories* such as atomistic density functional theory (DFT) for the computation of adsorption isotherms in simple pore geometries such as slits [15] or cylindrical capillaries [16]: This category also includes integral equation methods for porous matrices [17] and templated porous materials [18].
3. *Semiempirical models* such as the Horvath–Kawazoe (HK) method [19] and the Dubinin model [20] and their derivatives: These models generally make specific assumptions regarding the shape of the pores and/or the distribution function that describes the pore sizes within the adsorbent. To varying degrees, the semiempirical methods incorporate adsorbate–adsorbent interaction energies into the calculation of the theoretical isotherm.
4. *Classical thermodynamic models* of adsorption based upon the Kelvin equation [21] and its modified forms: These models are constructed from a balance of mechanical forces at the interface between the liquid and the vapor phases in a pore filled with condensate and, again, presume a specific pore shape. The Kelvin-derived analysis methods generate model isotherms from a continuum-level interpretation of the adsorbate surface tension, rather than from the atomistic-level calculations of molecular interaction energies that are predominantly utilized in the other categories.

As a general rule, the more sophisticated and computationally demanding thermodynamic models yield a more realistic description of the adsorption process and, consequently, a more accurate characterization of the pore structure when used to analyze experimental adsorption data. However, even numerically intensive analysis methods such as GCMC simulation and DFT will yield erroneous pore structure results if the model is not properly posed. For example, large errors may result in the pore size distribution interpreted from nitrogen adsorption of an activated carbon using DFT if unrealistic values are selected for the nitrogen–carbon potential parameters [22]. Thus, accurate characterization of the pore volume of an adsorbent requires both a realistic adsorption model, obtained from one of the four previously noted categories, and a method of fitting the key adjustable parameters of the adsorption model (in most cases, the intermolecular potential parameters). A third complicating factor, one that may introduce additional uncertainty into the characterization results, is the numerical technique used to interpret the experimental isotherm in terms of the designated adsorption model. Regularization methods, for example, may have a profound effect on the computed physical properties of a porous adsorbent [23].

In the remainder of this paper, adsorption models for adsorbent characterization based upon both amorphous (disordered) and idealized (simple geometric) pore structures are reviewed. A description of the principal structure analysis methods in each of the four thermodynamic model categories is also provided, and applications of these methods are highlighted. In Section II, amorphous porous microstructure models are discussed; in Section III, idealized pore geometric models are surveyed. Finally, in Section IV a summary of the state of the art in porous material characterization is presented, with an assessment of the relative merits of the currently available analysis methods and a set of recommendations for future improvements to these adsorption models.

II. Disordered Structure Models

Pore structure analysis methods based upon realistic disordered microstructures may be classified into two types. In one approach, the experimental procedures used to fabricate the material are reproduced, to the greatest extent possible, via molecular simulation, and the resulting amorphous material structure is then statistically analyzed to obtain the desired structural information. In the other approach, adsorbent structural data (e.g., small-angle neutron scattering) is used to construct a model disordered porous structure that is statistically consistent with the experimental measurements. As in the first approach, molecular simulations can then be carried out using the derived model structure to obtain the structural characteristics of the original adsorbent.

Several examples follow of recent efforts to describe explicitly porous adsorbent materials using disordered structure models.

A. Porous Glasses

An illustration of the first type of amorphous material modeling is the use of quench molecular dynamics (MD) methods to mimic the spinodal decomposition of a liquid mixture of oxides, producing model porous silica glasses that are topologically similar to controlled pore glasses (CPGs) or Vycor glasses [24, 25]. In the quench MD simulations, a homogeneous binary mixture of a large number (10^5 to 10^6) of spherical atomic particles at an elevated temperature is subjected to a sudden decrease in temperature, causing phase segregation to occur as shown in Fig. 1. As the quenching time increases, the extent of phase segregation also increases. By removing the atoms associated with the discontinuous phase (i.e., the atomic species with the smaller mole fraction), an irregularly shaped, highly interconnected

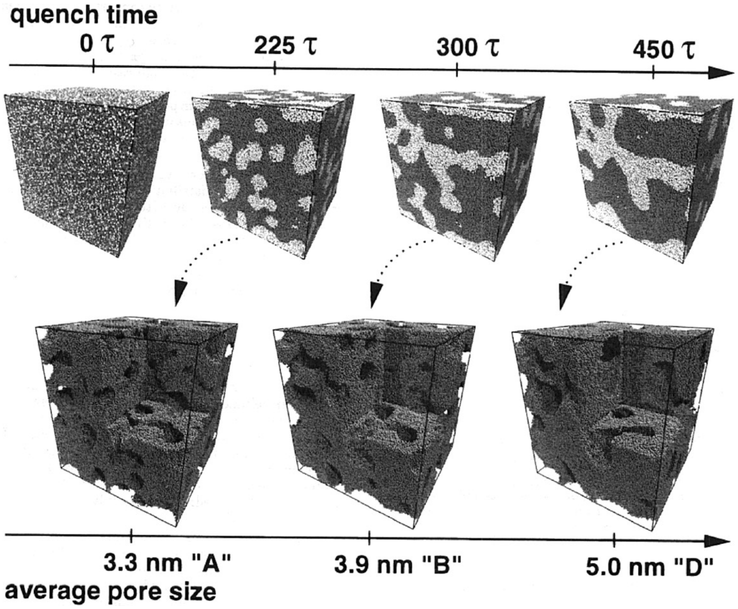

FIG. 1. Generation of model porous glasses using quench MD simulation of a binary mixture with a mole fraction of 0.70. Quenching produces a series of phase-separated structures, which may be converted at any time into a porous network (shown in cutaway view at the bottom) by removing the component with the smaller mole fraction [25].

network of pores is fashioned. For longer quenching times, larger phase segregated domains are formed as the binary mixture progresses toward the equilibrium phase-separated condition. This results in a larger average pore size in the porous network when the discontinuous phase is removed. By changing the quench time, the pore structure of the model adsorbent can therefore be tailored to some extent.

The quench MD procedure simulates the preparation of CPGs and Vycor glasses [26], in which the near-critical phase separation of a mixture of SiO_2, Na_2O, and B_2O_3, or a similar oxide mixture, is carried out, followed by etching to remove the borosilicate phase. The etching treatment produces a CPG silica matrix with a porosity ranging between 50 and 75% and an average pore size that is adjustable anywhere between 4.5 and 400 nm by varying the duration of the quenching stage. Vycor glasses prepared by a similar procedure have a porosity near 28% and an average pore diameter between 4 and 7 nm [27].

Once the model porous glass structures have been assembled using quench MD simulation, their geometric pore size distributions can be determined by sampling the pore volume accessible to probe molecules

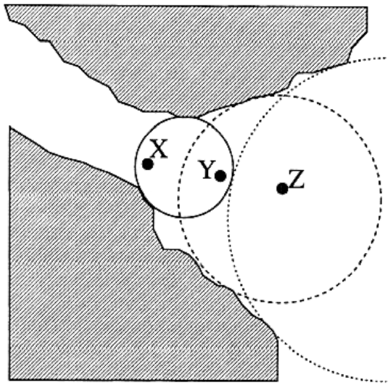

FIG. 2. Two-dimensional illustration of the geometric definition of the pore size distribution [25]. Point Z may be overlapped by all three circles of differing radii, whereas point Y is accessible only to the two smaller circles and point X is excluded from all but the smallest circle. The geometric pore size distribution is obtained by determining the size of the largest circle that can overlap each point in the pore volume. (Reproduced with permission from S. Ramalingam, D. Maroudas, and E. S. Aydil. Interactions of SiH radicals with silicon surfaces: An atomic-scale simulation study. *Journal of Applied Physics,* 1998;84:3895–3911. Copyright © 1998, American Institute of Physics.)

of different radii, as illustrated in Fig. 2. For each point in the pore volume, the radius of the largest spherical molecule is found which overlaps the given point but does not overlap any atoms of the solid matrix. For spherical probe molecules of radius r, there is a pore volume $V(r)$ that is accessible to the molecules. The pore volume function $V(r)$ is a monotonically decreasing function of r and is directly analogous to the cumulative pore volume curves commonly reported from interpretation of experimental adsorption isotherms [28]. The derivative $-dV(r)/dr$ is the fraction of the pore volume accessible to spheres of radius r but not accessible to spheres of radius $r + dr$. This derivative is a direct definition of the pore size distribution function and it can be calculated by Monte Carlo volume integration [29].

Using this technique, it has been shown that the model disordered adsorbents created using quench MD simulation have pore size distributions, porosities, and specific surface areas that closely resemble those of actual porous glasses. An advantage of the geometric pore size definition, as presented in Fig. 2, is that for irregularly shaped pore volumes this definition is fully applicable. In contrast, most analytic methods for obtaining the cumulative pore volume distribution from the experimental isotherm are based upon simple geometric pore models that bear little resemblance to the complex porous glass structures shown in Fig. 1.

To develop amorphous structure model for the direct interpretation of adsorption isotherms measured on CPGs and porous glasses, one could in principle assemble a sequential array of disordered structures from quench MD using different quenching times for each model structure. By carrying out GCMC molecular simulations (described in Section III) to construct the adsorption isotherm of each candidate structure, a representative porous glass model structure could then be selected as the one that gives the best agreement with the experimentally measured probe gas isotherm. This procedure may be computationally expensive and time-consuming, however, because of the large number of atoms required to generate realistic pore structures from the quench MD simulations. An alternative method that has been suggested for interpreting porous glass structures is to use off-lattice reconstruction methods [30, 31] to build realistic models of porous glasses. In this method, a model microstructure is identified based upon the volume autocorrelation function obtained from TEM data. A method similar in theme is the reverse Monte Carlo (RMC) technique of matching the structures of model disordered porous carbons to data obtained from small-angle X-ray or neutron scattering [32]. This method is an example of the second approach to molecular modeling of amorphous solids, and it is described in more detail in the next section.

B. MICROPOROUS CARBONS

Experimental radial distribution functions (RDFs) for the atoms in a porous solid may be obtained from the Fourier transform of the structure factor measured using small-angle X-ray or neutron scattering [33]. The RDF for carbon–carbon atomic pairs in a microporous carbon provides the experimental input for developing a model disordered carbon microstructure using RMC simulation. The RMC method follows the procedure of traditional Monte Carlo methods in that an initial atomic configuration is systematically changed through a well-defined stochastic procedure. The principal distinction between various Monte Carlo techniques is in the criteria used to accept or reject trial configurations. Rather than basing configuration acceptance on ensemble probability functions, as in the well-known Metropolis algorithm [34], new configurations are accepted in the RMC method based upon whether they improve the agreement of simulated structure correlation functions with experimental inputs.

A morphological model for microporous carbons has recently been reported [32] in which rigid aromatic sheets of sp^2 bonded carbon are randomly placed in a three-dimensional cubic simulation cell with periodic boundaries. A typical carbon plate has the structure shown in Fig. 3a. The plates are roughly aligned in the simulation cell, as illustrated in Fig. 3b, but with random variations in their angles of tilt. RMC simulation is carried out by sampling three types of changes to the carbon structure: (i) translation and

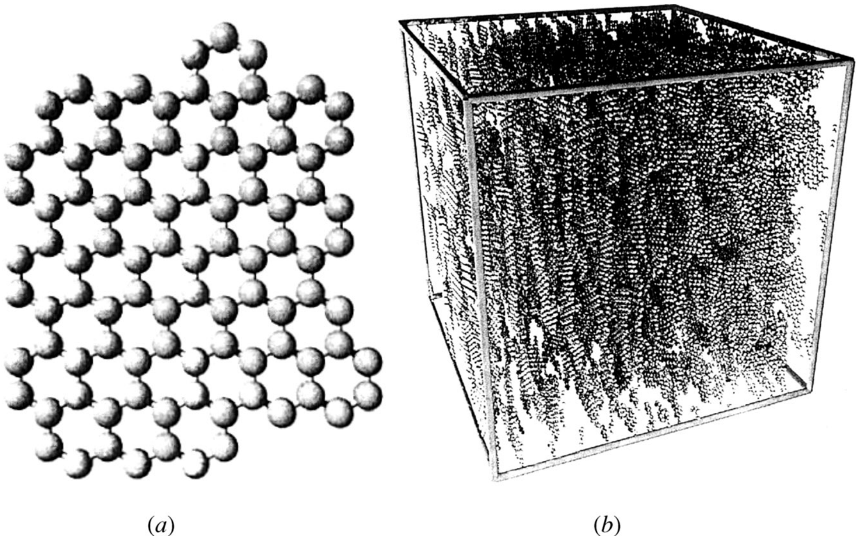

(*a*) (*b*)

FIG. 3. Structural representation of (a) a typical carbon plate and (b) a three-dimensional disordered carbon microstructure obtained from RMC simulation of a collection of carbon plates [32].

rotation of the plate centers of mass, (ii) addition or removal of aromatic rings from the edges of the carbon plates, and (iii) creation or annihilation of whole carbon plates. Sampled configurations are accepted if they bring the carbon–carbon radial distribution function $g(r)$ of the simulated structure into closer agreement with the experimental target distribution $g_{\mathrm{exp}}(r)$. The objective acceptance criterion χ^2 is given as

$$\chi^2 = \sum_{i=1}^{n} [g(r_i) - g_{\mathrm{exp}}(r_i)]^2, \tag{1}$$

where the range of separation distances over which RDF matching is to be carried out has been divided into n equally spaced intervals. A trial structure is accepted if $\chi^2_{\mathrm{new}} < \chi^2_{\mathrm{old}}$.

The RMC procedure has been used to study the structural morphology of microporous carbons. Porous carbons such as activated carbons, carbon fibers, carbon blacks, and vitreous carbons are often envisioned as disordered arrangements of defective crystallites of graphite [35]. The size and shape of the graphite crystallites are known to vary according to the ability of the material to transform to graphite under severe heat treatment. Domains of orientational order are usually observed in which microcrystallites align in similar direction [36]. A variety of models has been suggested to try to account for the deviations of activated carbon morphologies from

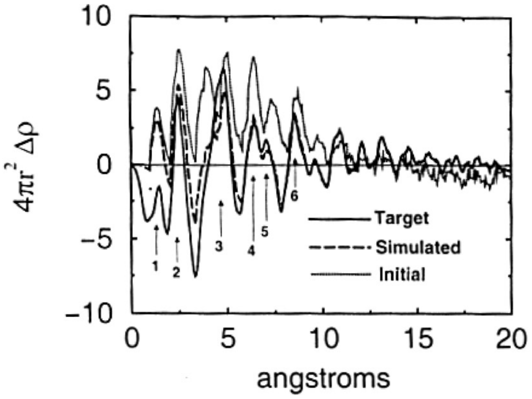

FIG. 4. Experimental (target) and simulated carbon–carbon radial distribution function for an activated mesocarbon microbead adsorbent [32]. The RDFs are reported in the form $4\pi r^2\rho[g(r) - 1]$, where ρ is the average carbon density and r is the carbon pair separation distance noted on the horizontal axis. The simulated RDFs for the initial and converged (dashed line) model structures are shown, with numbered peaks referenced in the text.

ideal slit-shaped pore geometries [10, 37–40]; none of these models, however, provides a method for constructing the model carbon microstructure from the experimental isotherm or scattering data. The RMC method, on the other hand, generates disordered structures that realistically simulate the structure correlation functions of carbon adsorbents.

Figure 4 shows a comparison between the simulated and the experimentally measured carbon–carbon RDFs for an activated mesocarbon microbead (MCMB) [32]. Using the RMC algorithm, the RDF of the initial adsorbent structure is brought into nearly exact agreement with the experimental RDF of the MCMB, determined from small-angle X-ray scattering (SAXS), for C—C distances greater than 7 Å. The differences between the best-fit simulated RDF and the experimental RDF below 5 Å are attributed to inaccuracies in the SAXS resolution of the structure factor. The RDFs in Fig. 4 combine both the intraplate and the interplate contributions to the C—C radial distribution function, the former comprising carbon atom pairs on the same plate and the latter from pairs located on different plates. The RDF for separation distances less than 5 Å corresponds almost exclusively to intraplate contributions, and SAXS experiment tends to undercount the carbon density in this portion of the measurement. The first RDF peak (labeled 1) represents the direct intraplate C—C distance along sp^2 bonds. Peaks 2 and 3 correspond to C—C distances for atom pairs in the same aromatic ring and in neighboring rings. Peak 3 also contains a contribution due to interplate separations between neighboring plates that are aligned

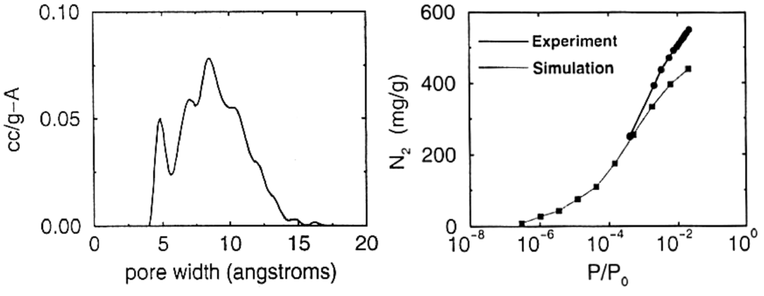

(*a*) (*b*)

FIG. 5. (a) Geometric pore size distribution calculated for the disordered carbon plate model of an activated MCMB adsorbent. (b) Comparison of experimental (circles) and simulated (squares) nitrogen adsorption isotherms at 77 K on activated MCMB [32].

nearly in parallel (i.e., stacked layers of graphitic crystallites). Peaks at larger separation distances correspond to specific interplate C—C distances; e.g., Peak 6, at 8.2 Å, is due primarily to second-nearest-neighbor interplate distances.

The geometric pore size distribution (PSD) can be found for the disordered porous carbon model structures using the same procedure as described for CPGs in Section II.A. The PSD so obtained for the converged simulated MCMB structure is shown in Fig. 5a. There is a direct correspondence between certain peaks in the PSD and peaks in the adsorbent RDF. For example, the PSD peak at ~5 Å arises from a staggered configuration of three stacked plates, in which the two outer plates extend beyond the end of the middle plate. This plate configuration yields a pore space approximately 5 Å in width and is observed throughout the MCMB structure shown in Fig. 3b.

The porosity, specific surface area, and micropore size distributions of the simulated model carbon structures are in good agreement with the physical properties of the target structures fitted using RMC simulation [32]. Another test of the RMC-derived structure is to calculate the nitrogen adsorption isotherm of the model structure at 77 K using grand canonical Monte Carlo simulation [41] (see Section III.A) and compare it with the experimental nitrogen isotherm. The result for the MCMB adsorbent is shown in Fig. 5b. It can be seen that the experimental and simulated isotherms are in excellent agreement for relative pressure P/P_0 below $\sim 10^{-3.3}$. At higher relative pressures, the simulated isotherm predicts a lower nitrogen uptake than the experimental result. This is due to the absence of mesopores in the simulated model structure, which condense nitrogen at relative pressures $P/P_0 > 10^{-3}$. There is no direct means of incorporating mesoporous structures into the RMC model because the structure correlation function $g(r)$ of the adsorbent material has a weak sensitivity to long-range correlations (see Fig. 4 for $r > 15$Å). One possible route for incorporate mesopore-sized void regions in the disordered model structure would be to include correlation functions in the RMC optimization that are specifically sensitive to long-range structure, such as those obtained from TEM micrographs. It should also be recognized that the optimized structure for MCMB shown in Fig. 3b, while consistent with the experimental structure and adsorption measurements, is by no means a unique solution to the adsorbent structure. Other carbon microstructures may be generated using the RMC technique, and these alternative structures will be equally consistent with the modeling constraints. In the case of purely graphitic crystalline models, variations among the plausible microstructures may not significantly effect the calculated adsorption properties. However, this may not necessarily be the case for more sophisticated models that incorporate plate defects or that include heteroatoms, such as oxygen-, nitrogen-, sulfur-containing surface functional groups that bridge between carbon plates. In the latter case, these factors may be expected to have significant effects on the pore morphology and adsorption properties.

C. XEROGELS

Capillary condensation and hysteresis have been investigated in disordered porous materials that resemble silica xerogels using GCMC molecular simulation [42–44]. In GCMC simulation of adsorption, configurational sampling of the adsorbate is carried out at a fixed chemical potential, temperature, and volume using three types of perturbations: (i) displacement of molecules to new positions, (ii) insertion of new molecules into the pore volume, and (iii) deletion of molecules from the pore volume. The displacement trial moves provide thermal equilibration of the fluid and are accepted with a probability p_{dis} given as

$$p_{\text{dis}} = \min\left[1, \exp\left(\frac{-\Delta U}{kT}\right)\right], \tag{2}$$

where k is the Boltzmann constant and T is the temperature. The configurational energy change ΔU associated with the molecular displacement includes both adsorbate–adsorbate and adsorbate–adsorbent potential interactions. The insertion and deletion trial configurations provide material equilibration at imposed chemical potential μ and are accepted with respective probabilities p_{ins} and p_{del} that depend on the current number of molecules N in the simulated pore volume according to the equations

$$p_{\text{ins}} = \min\left[1, \left(\frac{a}{N+1}\right)\exp\left(\frac{-\Delta U}{kT}\right)\right], \tag{3}$$

$$p_{\text{del}} = \min\left[1, \left(\frac{N}{a}\right)\exp\left(\frac{-\Delta U}{kT}\right)\right], \tag{4}$$

where

$$a = \left(\frac{h^2}{2\pi mkT}\right)\exp\left(\frac{\mu}{kT}\right), \tag{5}$$

and h and m are the Planck constant and the adsorbate molecular weight, respectively. The adsorption isotherm is constructed from GCMC simulation by statistically sampling the density of the equilibrated confined fluid for a sequence of chemical potential values, which can be related to the relative pressure through the appropriate bulk fluid equation of state (e.g., Ref. 45). By increasing the chemical potential in increments and computing the adsorbate density at each potential value, the adsorption branch of the isotherm is obtained; similarly, the desorption branch of the isotherm is recovered by computing the adsorbate density for a decreasing series of input chemical potential values.

The GCMC simulation method has been applied to the study of adsorption in model silica gels, in which the material is represented as a disordered collection of solid spherical particles [46, 47]. Figure 6a shows visualizations of the coexisting liquid and vapor phases of a Lennard–Jones fluid in a disordered array of spherical particles of uniform size [44]. The disordered model silica structure was obtained by equilibrating an ordered face-centered cubic array of spherical particles with the desired porosity (shown at the right in Fig. 6a) using molecular dynamics simulation. The effects of disorder may be discerned by comparing the isotherms obtained for the ordered and the amorphous structures. Figure 6b shows subcritical methane adsorption and desorption isotherms for two values of the methane–silica potential interaction strength. A hysteresis loop is seen that bears a resemblance to the category H2 loop in the IUPAC classification of type IV and type V isotherms observed for mesoporous solids [48]. This hysteresis is purely thermodynamic in nature; another manifestation of sorption hysteresis, arising from pore blocking effects in porous networks, may be investigated using the grand canonical molecular dynamics simulation technique [44, 49, 50].

The GCMC adsorption simulation method, when applied to model disordered assemblies of spherical silica particles, yields isotherms that are similar to the experimental isotherms of silica xerogels [51]. In principle,

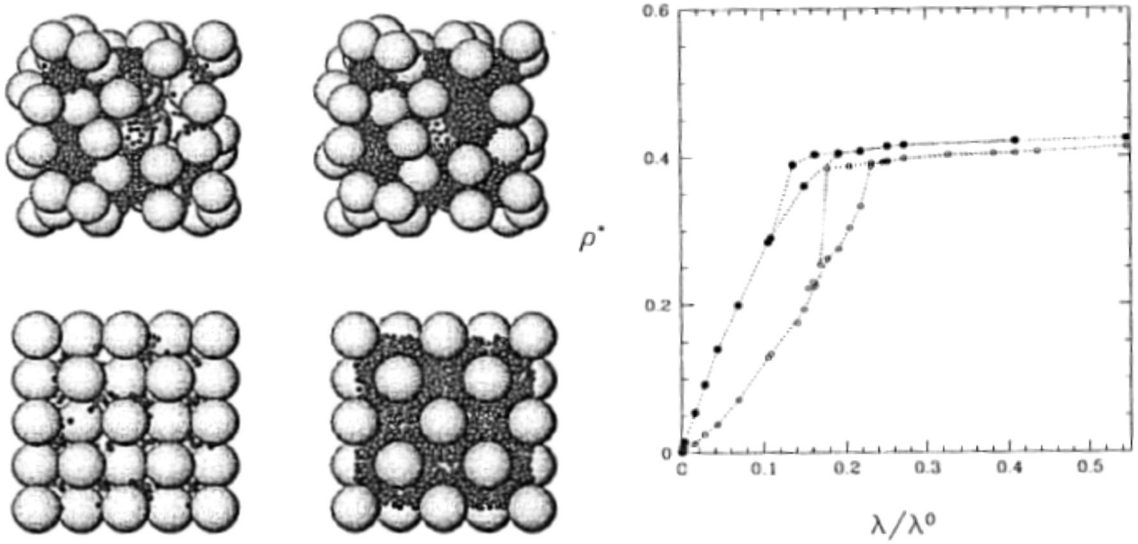

(a) (b)

Fig. 6. (a) Visualizations of configurations from GCMC simulations of confined fluids in model silica xerogels [44]. The small spheres are fluid molecules, and the large spheres are immobile silica particles. The top visualizations are for a disordered material and the bottom visualizations are for an ordered material of the same porosity. The visualizations on the left are for the saturated vapor state, and those on the right are for the corresponding saturated liquid state. (b) Simulated adsorption and desorption isotherms for Lennard–Jones methane in a silica xerogel at reduced temperature $kT/\varepsilon_{\mathrm{ff}} = 0.7$. The reduced adsorbate density $\rho^* = \rho\sigma^3$ is plotted vs the relative pressure λ/λ_0 for methane–silica/methane–methane well depth ratios $\varepsilon_{\mathrm{sf}}/\varepsilon_{\mathrm{ff}} = 1.5$ (open circles) and 1.8 (filled circles) [44]. (Reproduced with permission from S. Ramalingam, D. Maroudas, and E. S. Aydil. Atomistic simulation study of the interactions of SiH_3 radicals with silicon surfaces. *Journal of Applied Physics,* 1999;86:2872–2888. Copyright © 1999, American Institute of Physics.)

structure correlation data from scattering experiments could be used in conjunction with the adsorption isotherm to construct model disordered structures for specific silica gel adsorbents, using the methodologies described in Section II.B for activated microporous carbons.

D. Templated Porous Materials

Another variation on the theme of quenched disordered structures noted in Section II.A is to employ a removable template such as an organic molecule, colloid, or metal ion during the synthesis of a porous material [52–54]. Following formation of the quenched material structure, as shown in Fig. 7, the template is removed, leaving behind a matrix of particles with a pore space that mimics, to some extent, the original template. Because templates of diverse size and shape are available, templating offers the prospect of designing porous materials whose architectures are tailored for specific applications.

Model templated structures can be assembled from Monte Carlo simulations of binary mixtures of matrix and template particles [55–57]. Upon removal of the template from the quenched equilibrated structure, a porous matrix is recovered with an enhanced accessible void volume for adsorption. GCMC simulation studies have established that the largest enhancement of adsorption uptake occurs when the template particles used to fashion the porous matrix are the same size as the adsorbate molecules for which the adsorbent is intended [55]. The enhanced adsorption capacity of the templated material relative to a nontemplated matrix is noticeable even for modest template particle densities [55].

A adsorption model for a templated porous material may be posed in terms of seven replica Ornstein–Zernicke (ROZ) integral equations [58–60] that relate the direct and total correlation functions, $c_{ij}(r)$ and $h_{ij}(r)$, respectively, of the matrix–adsorbate system

$$h_{00} = c_{00} + \rho_0 c_{00} \otimes h_{00} + \rho_{0'} c_{00'} \otimes h_{00'} \tag{6}$$

$$h_{00'} = c_{00'} + \rho_0 c_{00} \otimes h_{00'} + \rho_{0'} c_{00'} \otimes h_{0'0'} \tag{7}$$

$$h_{0'0'} = c_{0'0'} + \rho_0 c_{00'} \otimes h_{00'} + \rho_{0'} c_{0'0'} \otimes h_{0'0'} \tag{8}$$

$$h_{01} = c_{01} + \rho_0 c_{00} \otimes h_{01} + \rho_{0'} c_{00'} \otimes h_{0'1} + \rho_1 c_{01} \otimes h_{\mathrm{c}} \tag{9}$$

$$h_{0'1} = c_{0'1} + \rho_0 c_{00'} \otimes h_{01} + \rho_{0'} c_{0'0'} \otimes h_{0'1} + \rho_1 c_{0'1} \otimes h_{\mathrm{c}} \tag{10}$$

$$h_{11} = c_{11} + \rho_0 c_{01} \otimes h_{01} + \rho_{0'} c_{0'1} \otimes h_{0'1} + \rho_1 c_{\mathrm{c}} \otimes h_{11} + \rho_1 c_{\mathrm{b}} \otimes h_{\mathrm{c}} \tag{11}$$

$$h_{\mathrm{c}} = c_{\mathrm{c}} + \rho_1 c_{\mathrm{c}} \otimes h_{\mathrm{c}}. \tag{12}$$

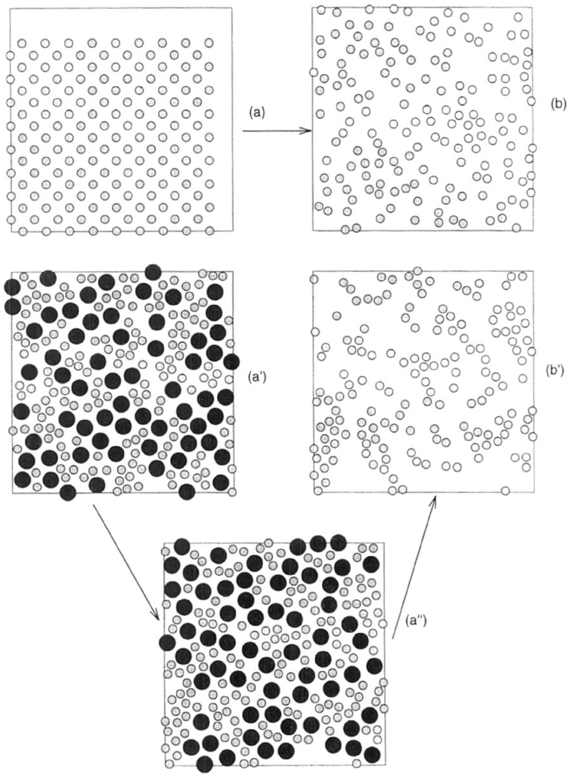

FIG. 7. Illustration of porous matrix formed via templating. The initial configuration of particles shown in a is equilibrated at a high temperature without a template and then quenched to yield the structure shown in b. The initial configuration in a′ has the same density of matrix particles (small circles) as in a, but template particles (large circles) are also present in this system. The template particles are removed from the quenched equilibrated matrix + template system (a′′) to yield the structure shown in b′. It is clear to the eye that the structure in b′ possesses a more "open" pore structure with more available void volume than the structure in b [55]. (Reproduced with permission from S. Ramalingam, D. Maroudas, and E. S. Aydil. Atomistic simulation study of the interactions of SiH_3 radicals with silicon surfaces. *Journal of Applied Physics,* 1999;86:2872–2888. Copyright © 1999, American Institute of Physics.)

In Eqs. (6)–(12), ρ_i is the density of component i; $\otimes$ denotes a convolution in r-space; and the subscripts $0, 0'$, and 1 refer to the matrix, template, and adsorbate, respectively. The subscript c denotes the correlation function between a pair of fluid particles whose graphical expansion results in diagrams that all possess at least one path involving only fluid particles. The subscript b, in contrast, refers to diagrams containing only paths that pass through at least one matrix particle. Solving the integral equations requires specification of

(i) a pairwise additive potential $u_{ij}(r)$, e.g., the hard-sphere potential, and (ii) a set of closures, such as the well-known Percus–Yevick closure [61],

$$c_{ij}(r) = [1 - \exp(u_{ij}(r)/kT)]\,[h_{ij}(r) + 1]\,. \tag{13}$$

Once the correlation functions have been solved, adsorption isotherms can be obtained from the Fourier transform of the direct correlation function $c_{\mathrm{c}}(r)$ [55]. The ROZ integral equation approach is noteworthy in that it yields model adsorption isotherms for disordered porous materials that have irregular pore geometries without resort to molecular simulation. In contrast, most other disordered structural models of porous solids implement GCMC or other simulation techniques to compute the adsorption isothem. However, no method has yet been demonstrated for determining the pore structure of model disordered or templated structures from experimental isotherm measurements using integral equation theory.

III. Simple Geometric Pore Structure Models

The severe computational burden associated with assembling and carrying out adsorption calculations on disordered model microstructures for porous solids, such as those discussed in Sections II.A and II.B, has until recently limited the development of pore volume characterization methods in this direction. While the realism of these models is highly appealing, their application to experimental isotherm or scattering data for interpretation of adsorbent pore structure remains cumbersome due to the structural complexity of the models and the computational resources that must be brought to bear in their utilization. Consequently, approximate pore structure models, based upon simple pore shapes such as slits or cylinders, have been retained in popular use for pore volume characterization.

The most commonly used approximate model for pore topology is to represent the pore volume of the adsorbent as an array of independent, chemical homogeneous, noninterconnected pores of some simple geometry; usually, these are slit-shaped for activated carbons and cylindrical-shaped for glasses, silicas, and other porous oxides. Usually, the heterogeneity is approximated by a distribution of pore sizes, it being implicitly assumed that all pores have the same shape and the same surface chemistry. In this case, the excess adsorption, $\Gamma(P)$, at bulk gas pressure P can be represented by the adsorption integral equation

$$\Gamma(P) = \int_{H_{\min}}^{H_{\max}} \Gamma(P, H) f(H) dH, \tag{14}$$

where the local isotherm $\Gamma(P, H)$ is the specific excess adsorption for an adsorbent in which all the pores are of size H; and $f(H)$ is the pore size distribution (PSD), such that $f(H)\ dH$ is the fraction of pores with sizes between H and $H + dH$. The integration is taken over all pore sizes between the minimum and the maximum pore sizes, $H_{\min}$ and $H_{\max}$, present in the adsorbent. Equation (14) assumes either that geometric and chemical heterogeneity are entirely absent or that they can be treated as effectively equivalent to pore size heterogeneity with regard to adsorption. An alternative approach [62] is to approximate the heterogeneity as due exclusively to chemical heterogeneity, with a distribution of adsorbate–adsorbent interaction energies $f(\varepsilon)$ such that Eq. (14) is replaced by

$$\Gamma(P) = \int_{\varepsilon_{\min}}^{\varepsilon_{\max}} \Gamma(P, \varepsilon) f(\varepsilon) d\varepsilon, \tag{15}$$

where $\Gamma(P, \varepsilon)$ is the local isotherm for pores with a uniform surface interaction energy ε.

At the level of approximation invoked by the simple geometric model, the mathematical problem becomes one of inverting Eq. (14), a linear Fredholm integral equation of the first kind, to obtain the PSD. The kernel $\Gamma(P, \varepsilon)$ represents the thermodynamic adsorption model, $\Gamma(P)$ is the experimental function, and the pore size distribution $f(H)$ is the unknown function. The usual method of determining $f(H)$ is to solve Eq. (14) numerically via discretization into a system of linear equations,

$$\sum_{j=1}^{m} \Gamma(P_i, H_j) \Delta H_j\, f(H_j) = \Gamma(P_i), \tag{16}$$

where the interval of pore sizes between $H_{\min}$ and $H_{\max}$ has been partitioned into m intervals, and $f(H_j)$ is a histogram coefficient that represents the fraction of pores with sizes ranging between $H_j - \Delta H_j/2$ and $H_j + \Delta H_j/2$. If the experimental isotherm is fitted at n different bulk gas pressures, then Eq. (16) yields a system of n linear equations in m unknowns. Such a system can be solved by minimizing the residual error, e.g., by a least-squares match to the experimental isotherm,

$$E = \sum_{i=1}^{n} \left[\Gamma(P_i) - \sum_{j=1}^{m} \Gamma(P_i, H_j) \Delta H_j\, f(H_j) \right]^2, \tag{17}$$

with the solution vector of coefficients $f(H_j)$ sought that minimizes the value of E. Alternatively, one may assign a nonnegative functional form to the PSD, such as a Gaussian distribution or a multimodal Γ distribution, and then fit the shape Γ parameters of the distribution so as to minimize the residual error given by Eq. (17). A variety of numerical minimization techniques may be used to carry out this task [63].

Fredholm integral equations are by nature numerically ill posed [64]. This means that experimental errors in the measurement of $\Gamma(P)$ may be transmitted to the unknown result $f(H)$ in such a way that the PSD is completely distorted. Application of the least-squares minimization method of Eq. (17) may in some cases lead to strong oscillations in the function $f(H)$, obscuring the true adsorbent PSD. The ill-posed nature of Eq. (14) is of mathematical origin and is not due to incorrect formulation of the physical problem. To circumvent the problems caused by the ill-posedness of the Fredholm integral equation, one may either (i) postulate an analytical form of the unknown function $f(H)$, as noted earlier, and find its parameter values via least-squares fitting [15]; (ii) fit an analytical equation to the experimental isotherm $\Gamma(P)$ that gives an analytical solution of integral equation and fit the coefficients of $f(H)$ via least squares; or (iii) use a regularization method to introduce an additional set of constraints into the solution of the adsorption integral equation, thus stabilizing the PSD with respect to perturbations in the experimental data [65–67]. The latter method involves the selection of constraints that are physically consistent with the expected form of the PSD. The most commonly adopted regularization procedure [68, 69] is to modify the objective function of Eq. (17) by adding a term that is proportional to the square of the second derivative of the pore size distribution function $f(H)$,

$$E = \sum_{i=1}^{n} \left[\Gamma(P_i) - \sum_{j=1}^{m} \Gamma(P_i, H_j) \Delta H_j \, f(H_j) \right]^2 + \alpha \sum_{j=1}^{m} \Delta H_j \left[f''(H_j) \right]^2 , \tag{18}$$

where the proportionality coefficient $\alpha > 0$ is referred to as the smoothing parameter. Essentially, regularization forces a slightly worse fit to the experimental isotherm $\Gamma(P)$ to generate a smoother PSD, under the presumption that the adsorbent is most likely to exhibit a relatively smooth distribution of pore sizes, centered around a few dominant pore sizes [68]. Figure 8 shows the effect of regularization for a range of smoothing parameter values employed in fitting the PSD of activated carbon to methane adsorption data using the objective function given by Eq. (18) [69]. It can be seen that as the calculated PSD becomes smoother, as expected, as the value of the smoothing parameter increases. The PSD progresses from a tetramodal distribution for $\alpha = 1$ to a unimodal distribution for $\alpha \geq 100$. To select which PSD is the "correct" PSD, one must consider the error bounds associated with the experimental measurements. If the experimental error is small, the tetramodal PSD shown in Fig. 8 may indeed be the correct PSD. However, if there is a greater uncertainty in the measured values of the experimental isotherm, then it is equally plausible that the PSD is unimodal, bimodal (e.g., $\alpha = 10$) or tetramodal in shape. One criterion that has been suggested for selecting

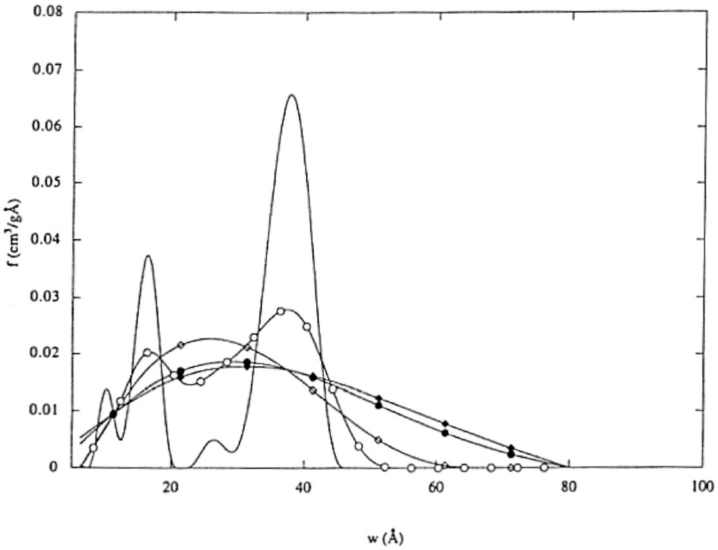

Fig. 8. PSDs obtained for methane adsorption in square model carbon pores using molecular simulation to interpret an activated carbon isotherm. PSD results are shown for regularization smoothing parameter values of 1 (solid line), 10 (open circles), 100 (open diamonds), 600 (filled circles), and 800 (filled diamonds) [69].

the proper PSD is to accept the smoothest distribution (i.e., largest value of α) to within the experimental error of the isotherm measurement [69].

A consequence of the ill-posed nature of Eq. (14), therefore, is that different PSD results can be obtained for the same material if different methods are applied to solve the adsorption integral equation, even if the same experimental data and adsorption model are used in both cases. A standard protocol has not yet been agreed upon for the use of regularization in pore size characterization. To avoid confusion in comparing PSD results, therefore, the numerical method employed to solve for the PSD and the type of regularization, if any, implemented to smooth the PSD should both be clearly identified.

Duly recognizing the potential pitfalls associated with inversion of the adsorption integral equation, the determination of the PSD reduces to the problem of selecting an adsorption model that represents the uptake of adsorbate in pores of different sizes that have the same shape and surface composition. This is a critical choice because the PSD results obtained from the inversion of Eq. (14) are highly sensitive to the selected adsorption model. As noted in Section I, adsorption models for simple geometric pore shapes can be categorized into four classes, based on the computational method used to generate the local adsorption isotherm for the model pore geometry. In the remainder of this section, selected examples from the four principal types of adsorption models are reviewed and discussed.

A. MOLECULAR SIMULATION ADSORPTION MODELS

GCMC simulation has been used to generate model isotherms for the adsorption of methane at supercritical temperatures [70] and the adsorption of carbon dioxide at subcritical temperatures [71] in slit-shaped carbon pores. The methane adsorbate is typically represented as a spherical Lennard–Jones molecule, whereas a three-center Lennard–Jones model is frequently used to represent the potential interactions of carbon dioxide [71, 72], with electrostatic point charges on the atoms to account for the CO_2 quadrupole. Adsorbate interactions with the carbon slit pore surfaces are most often modeled using the 10–4–3 potential in which the adsorbent is treated as stacked graphitic planes of Lennard–Jones atoms [73]. To determine activated carbon pore size distributions, GCMC model isotherms must usually be calculated for a set of one or two dozen slit pore widths spanning the micropore and mesopore size range between 7 and 50 Å. At the cryogenic temperatures used for nitrogen or argon porosimetry (77 or 87 K), adsorbate diffusion may be slow in carbon micropores, and long equilibration times may thus be required to measure the experimental adsorption isotherm. In such cases, the use of carbon dioxide or methane model isotherms at elevated temperatures (e.g., 195.5 or 273 K for CO_2, 308 K for methane) is an effective means of reducing mass transfer resistances in the adsorbent microstructure. For supercritical methane, however, the GCMC model can be used to determine only micropore PSDs, because the excess isotherms for methane adsorption are indistinguishable for pores larger than 20 Å [70].

A method of using GCMC simulation in conjunction with percolation theory [74, 75] has been suggested for simultaneous determination of the PSD and network connectivity of a porous solid [76]. In this method, isotherms are measured for a battery of adsorbate probe molecules of different sizes, e.g., CH_4, CF_4, and SF_6. As illustrated in Fig. 9a, the smaller probe molecules are able to access regions of the pore volume that exclude the larger adsorbates. Consequently, each adsorbate samples a different portion of the adsorbent PSD, as shown in Fig. 9b. By combining the PSD results for the individual probe gases with a percolation model, an estimate of the mean connectivity number of the network can be obtained [76].

An alternative molecular simulation technique for obtaining model adsorption isotherms for simple geometric pore structures is the Gibbs ensemble Monte Carlo (GEMC) simulation method [13, 22]. In GEMC simulation, configurational sampling is carried out between two simulation cells, (I) and (II), that represent regions of the pore volume. A schematic of the GEMC methodology for a slit-shaped pore geometry is shown in Fig. 10. Three types of sampling moves are performed in GEMC simulation: (a) displacement of molecules in each pore region; (b) interchange of

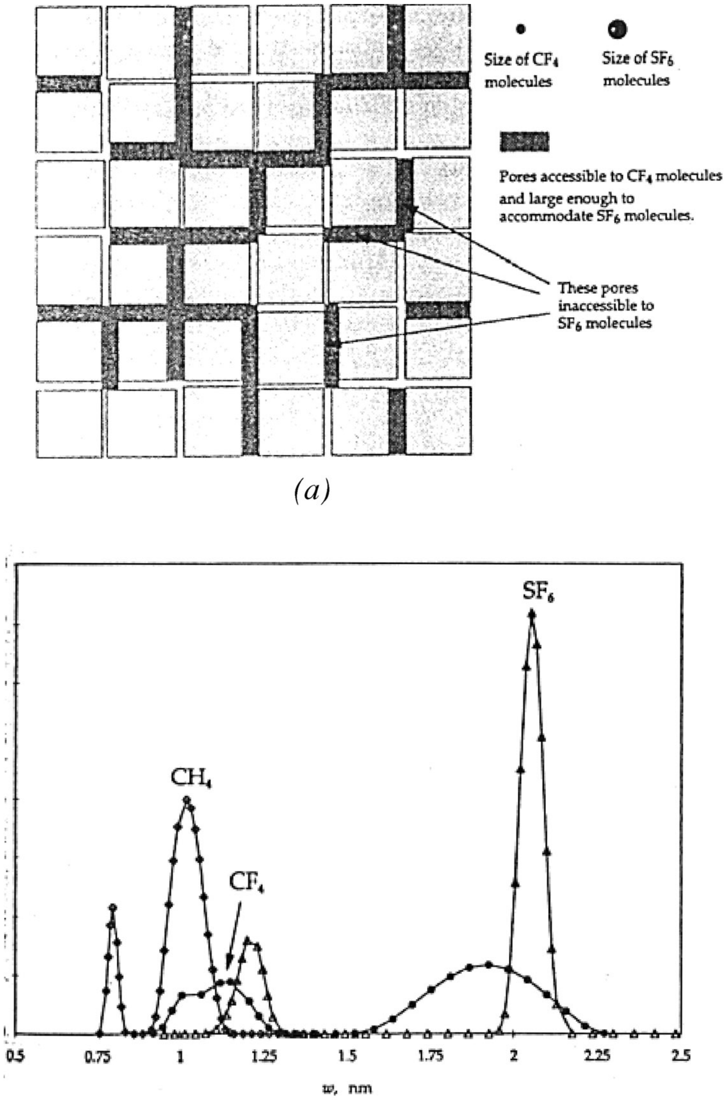

(a)

(b)

FIG. 9. (a) Schematic illustration of the connection between adsorption and percolation in a porous network. Some pores large enough to accommodate large adsorbate molecules (e.g., SF_6) remain unfilled because they cannot be accessed through smaller connecting pore channels. (b) PSD results obtained using GCMC simulation to interpret CH_4, CF_4, and SF_6 isotherms measured on an activated carbon at 296 K. The smaller probe molecules sample regions of the pore volume that are inaccessible to the large adsorbate molecules [76].

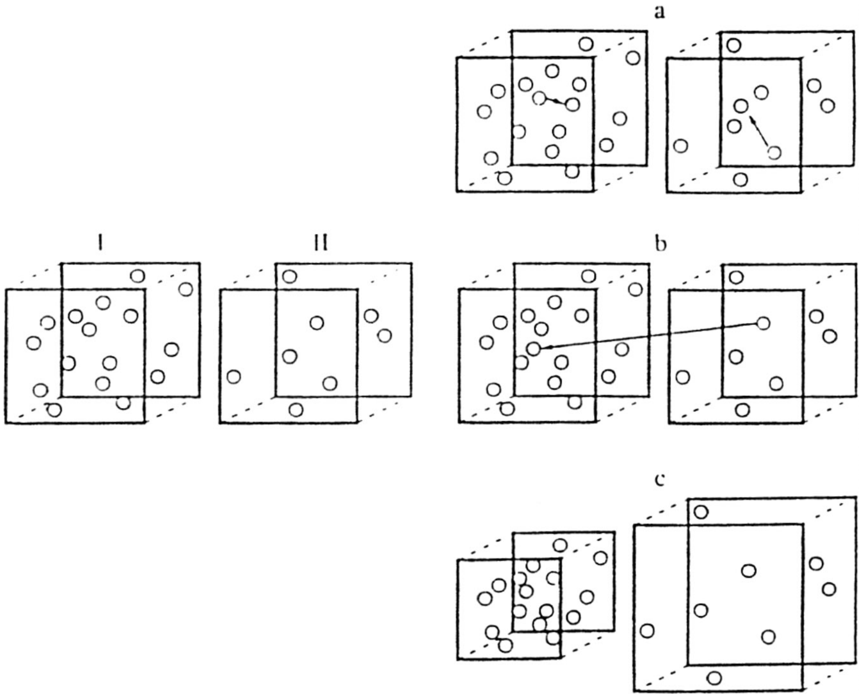

FIG. 10. Schematic of the Gibbs ensemble Monte Carlo simulation method for calculation of phase equilibria of confined fluids [22].

molecules between the two regions; and (c) exchange of pore volume between the two regions, with the total pore volume and the slit pore width held constant. The acceptance probabilities for the sampling moves are given as

$$p = \min\left[1, \exp\left(-\frac{\Delta U}{kT}\right)\right], \tag{19}$$

where the change in total energy ΔU depends on the type of perturbation. For molecular displacements,

$$\Delta U_{\text{dis}} = \Delta U_{\text{I}} + \Delta U_{\text{II}}, \tag{20}$$

where ΔU_i is the energy change that occurs in simulation cell i. For interchange steps,

$$\Delta U_{\text{int}} = \Delta U_{\text{I}} + \Delta U_{\text{II}} + kT \ln\left[\frac{(N_{\text{I}} + 1)V_{\text{II}}}{N_{\text{II}}V_{\text{I}}}\right], \tag{21}$$

where N_i and V_i are the number of molecules and volume, respectively, of simulation cell i. For volume exchange steps,

$$\Delta U_{\mathrm{vol}} = \Delta U_{\mathrm{I}} + \Delta U_{\mathrm{II}} - N_{\mathrm{I}} kT \ln\left(\frac{V_{\mathrm{I}} - \Delta V}{V_{\mathrm{I}}}\right) - N_{\mathrm{II}} kT \ln\left(\frac{V_{\mathrm{II}} + \Delta V}{V_{\mathrm{II}}}\right), \tag{22}$$

where ΔV is the amount of volume exchanged between the two simulation cells. Configurational sampling brings the two regions into thermal, material, and mechanical equilibrium, thus yielding the densities of the coexisting liquid and vapor states in the pore. GEMC simulations can also be carried out to obtain coexistence properties for an adsorbed fluid in equilibrium with a bulk vapor [13, 22]. By performing a series of GEMC simulations starting from different initial densities in the two simulation cells, the isotherm for a pore of prescribed width can be constructed. A distinct advantage of GEMC over GCMC simulation is that in the GEMC method, the chemical potential of the bulk vapor phase need not be specified as an input to the computer simulation. When the GEMC simulations are performed correctly, the pressures and chemical potentials of regions I and II will be the same at equilibrium. Thus, in GEMC the adsorption isotherm can be calculated without direct knowledge of the chemical potential. This is particularly useful for situations in which the bulk fluid equation of state is not known.

GEMC model isotherms have been constructed for nitrogen adsorption in slit-shaped carbon pores [22] and cylindrical oxide pores [11]. The filling pressure at which capillary condensation is expected to occur in a pore of given size can be extracted in a straightforward manner from GEMC calculations and the correlation is shown for the nitrogen–carbon system in Fig. 11. The pore filling correlations predicted by several other adsorption models for slit-shaped pores are also shown in Fig. 11. These models, and the reasons for the differences evident in Fig. 11, are discussed in the sections that follow.

B. DENSITY FUNCTIONAL THEORY ADSORPTION MODELS

The DFT method [15, 77–79] is derived from statistical thermodynamics and offers an efficient means of computing model isotherms for simple pore geometries. The accuracy of the DFT model isotherms rivals that of the isotherms obtained from molecular simulation, but the computational time required by DFT is typically about 1% of the CPU time needed to complete GCMC or GEMC isotherm calculations for a comparable system. The DFT method retains its computational advantage over molecular simulation only for pore shapes of low dimensionality, such as slits, spheres, or

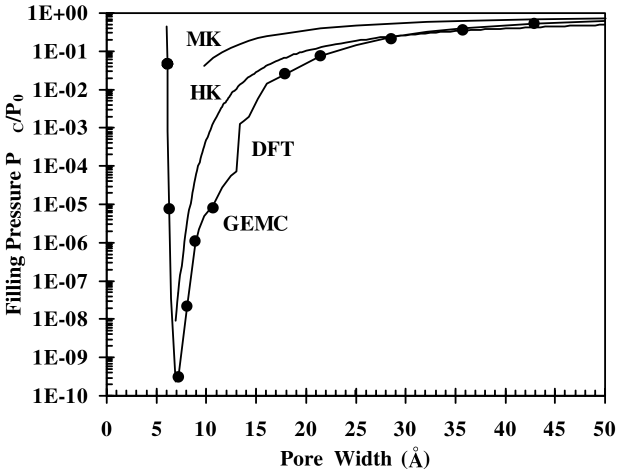

FIG. 11. Relationship between the pore filling pressure and the pore width predicted by the modified Kelvin equation (MK), the Horvath–Kawazoe method (HK), density functional theory (DFT), and Gibbs ensemble Monte Carlo simulation (points) for nitrogen adsorption in carbon slit pores at 77 K [11].

cylinders, so DFT is not applicable to realistic disordered structures such as those considered in Section II.

In the DFT method [80], each individual pore has a fixed geometry and is in open contact with the bulk vapor-phase adsorbate at a fixed temperature. For this system, the grand canonical ensemble provides the appropriate description of the thermodynamics. In this ensemble, the chemical potential μ, temperature T, and pore volume V are specified. In the presence of a spatially varying external potential V_{ext}, the grand potential functional Ω of the fluid is [15]

$$\Omega[\rho(\mathbf{r})] = F[\rho(\mathbf{r})] - \int d\mathbf{r}\rho(\mathbf{r})[\mu - V_{\text{ext}}(\mathbf{r})], \tag{23}$$

where F is the intrinsic Helmholtz free energy functional, $\rho(\mathbf{r})$ is the local fluid density at position $\mathbf{r}$, and the integration is carried out over the entire pore volume. The free energy functional is expanded to first order about a reference system of hard-sphere adsorbate molecules, with the temperature-dependent diameter d given by the Barker–Henderson prescription [81]

$$F[\rho(\mathbf{r})] = F_{\text{h}}[\rho(\mathbf{r}); d] + \frac{1}{2}\int\int d\mathbf{r}\, d\mathbf{r}'\rho(\mathbf{r})\rho(\mathbf{r}')\phi_{\text{att}}(|\mathbf{r} - \mathbf{r}'|), \tag{24}$$

where F_{h} is the hard-sphere Helmholtz free energy functional and ϕ_{att} is the attractive part of the adsorbate–adsorbate potential. Equation (24) invokes the mean field approximation, wherein pair correlations between molecules due to attractive forces are neglected. The attractive part of the adsorbate pair potential is represented using the WCA division of the Lennard–Jones potential [82],

$$\begin{aligned} \phi_{\mathrm{att}}(|\mathbf{r}-\mathbf{r}'|) = \phi_{\mathrm{ff}}(|\mathbf{r}-\mathbf{r}'|), \qquad & |\mathbf{r}-\mathbf{r}'| > r_{\mathrm{m}} \\ -\varepsilon_{\mathrm{ff}}, \qquad & |\mathbf{r}-\mathbf{r}'| < r_{\mathrm{m}}, \end{aligned} \tag{25}$$

where $r_{\mathrm{m}} = 2^{1/6}\sigma_{\mathrm{ff}}$ is the location of the minimum of the Lennard–Jones potential ϕ_{ff}, and $\varepsilon_{\mathrm{ff}}$ and σ_{ff} are the Lennard–Jones well depth and molecular diameter, respectively. The hard-sphere free energy functional F_{h} can be written as the sum of two terms,

$$F_{\mathrm{h}}[\rho(\mathbf{r}); d] = kT \int d\mathbf{r}\rho(\mathbf{r})[\ln(\Lambda^3\rho(\mathbf{r})) - 1] + kT \int d\mathbf{r}\rho(\mathbf{r}) f_{\mathrm{ex}}[\bar{\rho}(\mathbf{r}); d], \tag{26}$$

where $\Lambda = h/(2\pi mkT)^{1/2}$ is the thermal de Broglie wavelength, m is the molecular mass, h and k are the Planck and Boltzmann constants, respectively, and f_{ex} is the excess molar Helmholtz free energy, i.e., the total molar free energy less the ideal gas contribution. The excess molar free energy of the hard-sphere fluid is calculated from the Carnahan–Starling equation of state [83]. The first term on the right-hand side of Eq. (26) is the ideal-gas contribution, which is exactly local; i.e., its value at $\mathbf{r}$ depends only on $\rho(\mathbf{r})$. The second term on the right-hand side of Eq. (26) is the excess contribution, which is nonlocal and is calculated using a smoothed density, $\bar{\rho}(\mathbf{r})$, that represents a suitable weighted average of the local density $\rho(\mathbf{r})$

$$\bar{\rho}(\mathbf{r}) = \int d\mathbf{r}'\rho(\mathbf{r}')w[|\mathbf{r}-\mathbf{r}'|; \bar{\rho}(\mathbf{r})]. \tag{27}$$

The choice of the weighting function w depends on the version of DFT used. If the δ function is assigned for w, the smoothed density reverts to the local density and the so-called local DFT method is obtained [77]. The local DFT model correctly describes many of the structural features of inhomogeneous fluids but becomes inaccurate for fluids confined in small pores because of the strong short-ranged correlations present in such fluids. For highly inhomogeneous confined fluids, a smoothed or nonlocal density approximation is needed that gives a good description of the direct correlation function for the hard-sphere fluid over a wide range of fluid densities. Among the several weighting function sets that have been proposed [84–88], Tarazona's model [86–88] is the one most commonly used for the nonlocal version of DFT. This model has been shown to give very good agreement with simulation results for the density profile and surface tension of Lennard–Jones fluids near attractive surfaces. The Tarazona prescription for the weighting functions uses a power series expansion in the smoothed density, truncating at the second-order term

$$w[|\mathbf{r}-\mathbf{r}'|;\bar{\rho}(\mathbf{r})]=\sum_{i=0}^{2} w_j(|\mathbf{r}-\mathbf{r}'|)\bar{\rho}(\mathbf{r})^i. \tag{28}$$

The effect of the weighting is to flatten the sharp oscillations of the local density profile into a smoothed density profile that is input into the equation of state for the excess hard-sphere free energy. The nonlocal DFT method thus avoids difficulties associated with applying the equation of state to unrealistically large values of the local density, as is the case with the local DFT method.

The equilibrium density profile is determined by minimizing the grand potential functional with respect to the local density,

$$\frac{\delta\Omega[\rho(\mathbf{r})]}{\delta\rho(\mathbf{r})}=0 \qquad \text{at} \qquad \rho=\rho_{\text{eq}}. \tag{29}$$

An iteration scheme is used to numerically solve this minimization condition to obtain $\rho_{\text{eq}}(\mathbf{r})$ at the selected temperature, pore width, and chemical potential. For simple geometric pore shapes such as slits or cylinders, the local density is a function of one spatial coordinate only (the coordinate normal to the adsorbent surface) and an efficient solution of Eq. (29) is possible. The adsorption and desorption branches of the isotherm can be constructed in a manner analogous to that used for GCMC simulation. The chemical potential is increased or decreased sequentially, and the solution for the local density profile at previous value of μ is used as the initial guess for the density profile at the next value of μ. The chemical potential at which the equilibrium phase transition occurs is identified as the value of μ for which the liquid and vapor states have the same grand potential.

The DFT excess isotherm is found by taking the volume average of the local adsorbate density profile, e.g., for a slit-shaped pore of width H,

$$\Gamma(P,H)=\frac{1}{H}\int_0^H[\rho(z)-\rho_{\text{b}}]dz, \tag{30}$$

where z is the spatial coordinate normal to the pore walls and ρ_{b} is the bulk vapor phase density at pressure P. The pressure may be obtained from the chemical potential using the bulk fluid equation of state [89].

DFT model isotherms have been reported for adsorption of nitrogen [15, 22, 77, 79, 90–93], argon [90–92], methane [93, 94], helium [93], and carbon dioxide [72, 92, 95] in slit-shaped graphitic carbon pores and adsorption of nitrogen [8, 11, 78, 96] and argon [8, 78] in cylindrical capillaries with oxide surfaces. Most of the DFT models are developed at cryogenic temperatures,

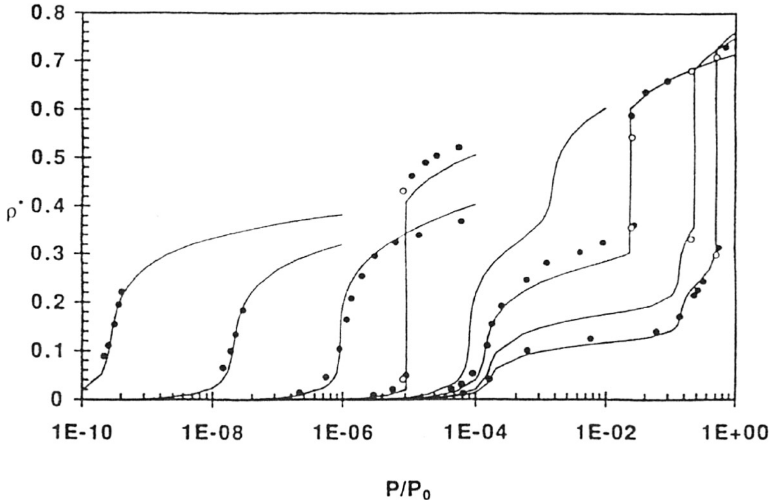

FIG. 12. Comparison of DFT (lines) and GEMC (points) model isotherms $\rho^* = \rho\sigma_{\mathrm{ff}}^3$ obtained for nitrogen adsorption at 77 K in slit-shaped carbon pores of width (reading from left to right) $H = 7.1, 8.0, 8.9, 10.7, 13.4, 17.9, 28.6$, and 42.9 Å [22].

where capillary condensation provides a distinct experimental "fingerprint" of the PSD. As noted in Section III.A, isotherm databases may also be constructed to interpret uptake measurements at elevated temperatures in cases where slow mass transfer is a concern.

Theoretical isotherms obtained using DFT method rival the accuracy of model isotherms constructed from molecular simulation, as shown in the comparison in Fig. 12 for N_2 adsorption results in model graphitic slit pores at 77 K [22]. The DFT model correctly predicts the capillary condensation pressure, the most prominent feature of the subcritical isotherm, relative to the exact computer simulation results shown in Fig. 11. DFT also provides a good description of the secondary structure of the mesopore isotherm (e.g., $H = 42.9$ Å in Fig. 12), in which capillary condensation may be preceded by one or more wetting transitions.

A test of the robustness of the DFT method is the consistency of the adsorbent PSDs calculated from adsorption experiments using different adsorbate molecules to probe the pore volume. Figure 13 shows a comparison of porosimetry results obtained using nitrogen and argon to probe the pore structures of activated carbons [90]. The specific pore volume, mean pore diameter, and PSD maximum obtained from nitrogen and argon porosimetry were all found to agree to within 8% for the two probe gases using DFT to interpret the adsorption isotherms measured for both species. The differences, where noted, may be ascribed in part to the heterogeneity of the carbon samples, which all possess an appreciable mass

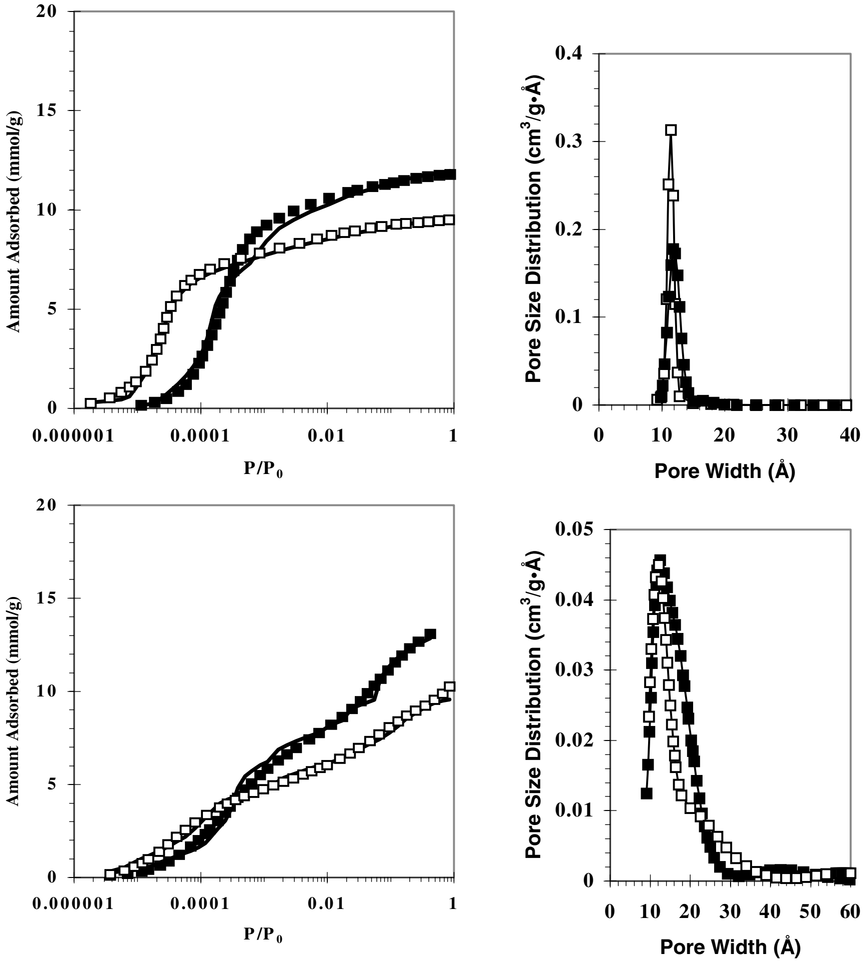

FIG. 13. Adsorption isotherms (left) and pore size distributions (right) computed from nitrogen (open squares) and argon (filled squares) adsorption at 77 K on a porous Saran char (top) and a granular activated carbon (bottom) [90]. (Reproduced with permission from S. Ramalingam. Plasma-surface interactions in deposition of silicon thin films: An atomic-scale analysis. PhD Thesis, University of California, Santa Barbara; 2000.)

fraction (9 to 13%) of hydrogen-, nitrogen-, oxygen-, and sulfur-containing surface functional groups [90]. These heteroatoms can interact with the nitrogen quadrupole and adsorb nitrogen at pressures lower than for N_2 adsorption on bare graphitic surfaces. Another study [94] reported similar findings for PSD differences between quadrupolar nitrogen and nonpolar methane on microporous carbons. For adsorbents that exhibit substantial chemical heterogeneity, the use of a probe molecule (e.g., argon) that has no permanent electrostatic moments is therefore recommended.

DFT-based pore size distribution results have also been reported for the family of templated siliceous mesoporous molecular sieves first synthesized by Mobil researchers [97] and designated M41S. The most well-known members of this family are MCM-41, which has a hexagonal array of unidirectional pores [98], and MCM-48, which has a cubic pore system [99]. The pore diameters of these adsorbents typically range between 30 and 40 Å. The PSDs of MCM-41 and MCM-48 adsorbents have been calculated to a high degree of consistency using a cylindrical oxide pore DFT model to interpret experimental nitrogen and argon isotherms, as shown in Fig. 14a for a MCM-41-type adsorbent [8]. By subtracting the DFT result for the internal pore diameter from X- ray diffraction measurement of the pore spacing, the pore wall thickness of an MCM-class adsorbent can be estimated. Figure 14b shows the wall thickness calculated for five MCM-41 adsorbents using the diffraction data in combination with the adsorption isotherm. The wall thicknesses, were found to be between 6 and 8 Å for four of the five adsorbents, consistent with other independent estimates of the wall thickness of MCM-41 materials obtained from transmission electron microscopy [100].

C. Semiempirical Adsorption Models

Two principal semiempirical adsorption models have enjoyed widespread use for adsorbent PSD characterization: the Horvath-Kawazoe (HK) method [19] and its derivatives, and approaches based upon the ideas of Dubinin [20] for modeling micropore distributions. Each of these methodologies is considered in turn.

1. The Horvath–Kawazoe Method

In the original HK method [19], an analytic pore filling correlation is obtained by calculating the mean free energy change of adsorption $\bar{\phi}$ that occurs when an adsorbate molecule is transferred from the bulk vapor phase to the condensed phase in a slit pore of width H

$$\ln(P_c/P_0) = \bar{\phi}(H)/kT. \tag{31}$$

In Eq. (31), P_0 is the saturation pressure and P_c is the pore condensation pressure. The assumed exponential dependence of the condensation pressure on the adsorption free energy change is similar in basis to the Polanyi potential theory [101] and the Frenkel–Halsey–Hill (FHH) theory [102–104]. In the HK method, the mean free energy change due to adsorption is calculated

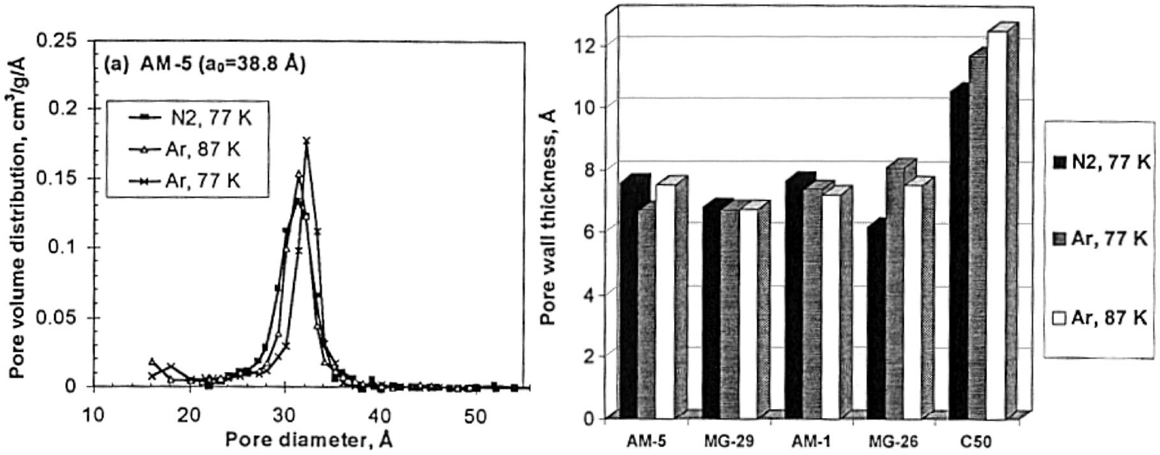

(a) *(b)*

FIG. 14. (a) PSDs obtained for MCM-41-type adsorbents from nitrogen and argon DFT porosimetry. (b) Pore wall thickness calculated for five MCM-41 adsorbents using a combination of X-ray diffraction data and N_2/Ar adsorption measurements [8].

from an unweighted average of the adsorbate interaction potential ϕ, measured over the slit pore volume between $z = \sigma_{\text{sf}}$ and $z = H - \sigma_{\text{sf}}$

$$\bar{\phi} = \frac{\int_{\sigma_{\text{sf}}}^{H-\sigma_{\text{sf}}} \phi(z)dz}{\int_{\sigma_{\text{sf}}}^{H-\sigma_{\text{sf}}} dz} = \frac{\int_{\sigma_{\text{sf}}}^{H-\sigma_{\text{sf}}} \phi(z)dz}{H - 2\sigma_{\text{sf}}}, \tag{32}$$

where z is the distance of the adsorbate center of mass from the surface layer plane of atomic nuclei, and σ_{sf} is the arithmetic mean of the adsorbate and adsorbent diameters. The interaction energy of the adsorbate molecule and the pore wall is represented by the sum of two 10–4 potentials, one that represents the adsorbate–adsorbent potential ϕ_{sf} and the other representing an effective adsorbate–adsorbate interaction ϕ_{ff}

$$\phi(z) = \phi_{\text{sf}}(z) + \phi_{\text{ff}}(z) = \frac{N_{\text{s}}A_{\text{sf}} + N_{\text{f}}A_{\text{ff}}}{2d^4}\left[\left(\frac{d}{z}\right)^{10} - \left(\frac{d}{z}\right)^{4} + \left(\frac{d}{H-z}\right)^{10} - \left(\frac{d}{H-z}\right)^{4}\right]. \tag{33}$$

In Eq. (33), N is the molecular density (i.e., molecules per unit surface area); A is the dispersion coefficient; the subscripts s and f refer to the adsorbent and adsorbate, respectively; and $d = (2/5)^{1/6}\,\sigma_{\text{sf}}$. The 10–4 potential is obtained by integrating the Lennard–Jones potential over an unbounded planar surface [105]. The dispersion coefficients are calculated using the Kirkwood–Muller equations (as reported in Ref. 19)

$$A_{\text{sf}} = \frac{6mc^2\alpha_{\text{s}}\alpha_{\text{f}}}{(\alpha_{\text{s}}/\chi_{\text{s}}) + (\alpha_{\text{f}}/\chi_{\text{f}})} \tag{34}$$

$$A_{\text{ff}} = \frac{3}{2}mc^2\alpha_{\text{f}}\chi_{\text{f}}. \tag{35}$$

In Eqs. (34) and (35), m is the mass of an electron, c is the velocity of light, and α and χ are the polarizability and the magnetic susceptibility, respectively. Substitution of Eqs. (32) and (33) into Eq. (31) and integration yields the HK correlation between the pore condensation pressure and the slit pore width

$$\ln\left(\frac{P_{\text{c}}}{P_0}\right) = \frac{N_{\text{s}}A_{\text{sf}} + N_{\text{f}}A_{\text{ff}}}{kTd^3(H - 2\sigma_{\text{sf}})}\left[\frac{1}{9}\left(\frac{d}{\sigma_{\text{sf}}}\right)^9 - \frac{1}{3}\left(\frac{d}{\sigma_{\text{sf}}}\right)^3 - \frac{1}{9}\left(\frac{d}{H-\sigma_{\text{sf}}}\right)^9 + \frac{1}{3}\left(\frac{d}{H-\sigma_{\text{sf}}}\right)^3\right]. \tag{36}$$

Correlations similar to Eq. (36) have been derived for cylindrical [106] and spherical [107] pore geometries and for adsorbates other than nitrogen, such as argon [108] and methyl chloride [109]. The analytic HK correlation may be conveniently applied to adsorbent PSD analysis using a simple spreadsheet, whereas a computer algorithm is required to obtain theoretical isotherms via DFT or molecular simulation.

In Fig. 11, the pore filling correlation predicted by Eq. (36) is shown for nitrogen adsorption in carbon slit pores at 77 K, using dispersion parameters reported in the original HK paper [19]. The HK method correctly predicts a sharp decrease in the pore filling pressure as the pore width decreases into the micropore range. This dramatic decrease occurs because of enhancement of the gas–solid potential in narrow slit pores, and the HK method qualitatively accounts for this effect. It is evident from Fig. 11, however, that the HK adsorption model, as originally posed, does not agree with the pore filling correlations obtained from DFT or GEMC simulation for the nitrogen–carbon system. The differences in the model results can be attributed to three causes.

(i) The HK model uses the 10–4 potential in the calculation of the adsorption free energy change, whereas DFT and molecular simulation models routinely represent the gas–solid potential using the 10–4–3 potential [73], which contains an additional attractive term for adsorbate interactions with the subsurface layers of adsorbent atoms.

(ii) The adsorbate–adsorbent dispersion parameter calculated using Eq. (34) in the original HK paper is considerably smaller than the comparable parameter obtained in the DFT and simulation models by fitting the model isotherm to a nonporous graphitized carbon reference adsorbent [22].

(iii) The adsorbate potential representation given by Eq. (33) is posed incorrectly. As noted in two recent publications [110, 111], in the FHH formulation, the adsorbate–adsorbate interaction is subtracted from the adsorbate–adsorbent interaction, rather than added to it as shown in Eq. (33). The theoretical construct of FHH theory is that a slab of adsorbate is removed and replaced with a slab of adsorbent atoms [102]. In the original HK treatment, the adsorbate–adsorbate interactions are, without justification, directly superimposed onto the adsorbate–adsorbent interactions in a physically implausible manner [110, 111]. Additionally, a factor of two error appears in the Kirkwood–Muller formula for the adsorbate dispersion coefficient A_{ff} reported in the original HK method [19]. As noted by Muller [112], the leading coefficient on the right-hand side of Eq. (34) should be 3 rather than 3/2.

It has been shown that much better agreement between the HK and the DFT pore filling pressure correlations is obtained if the same form of the gas–solid potential and the same potential parameter values are used in comparing the two models [111].

2. *Modified Horvath–Kawazoe Models*

Several modifications of the original HK method have been suggested to bring the semiempirical model into better agreement with DFT and GEMC results [110, 111, 113, 114]. One approach is to use weighting functions (e.g., a multimodal Gaussian distribution) to represent the spatial variations in the local density due to fluid layering near the pore walls [111, 113]. In this representation, the mean free energy change of adsorption is calculated as

$$\bar{\phi} = \frac{\int_d^{H-d} \rho(z)\phi(z)dz}{\int_d^{H-d} \rho(z)dz}, \tag{37}$$

where the integration is now weighted with respect to the local density $\rho(z)$. This approach yields lower pore filling pressures than are obtained from Eq. (32) because of the additional weighting toward the regions of the pore volume where the gas–solid potential is the most attractive (i.e., the monolayer well adjacent to each pore wall).

Another modification that has been suggested is a geometric approximation [110] in which different potentials are used to calculate the interaction energy of the adsorbate layer adjacent to the pore wall (molecules marked “A” in Fig. 15a) and adsorbate layers in the interior of the pore (molecules marked “B”). Type A molecules are assumed to interact with the surface adsorbent atoms on one side and with adsorbate molecules on the other side, whereas Type B molecules interact only with the two adjacent layers of adsorbate. This method of averaging does away with the integration of Eq. (32) and replaces it with a summation of the energies of molecules sited at discrete positions. The PSD results obtained from this modified HK model for molecular sieve carbons, aluminophosphates and zeolites were in better agreement with crystallographic data for these adsorbents than PSD results obtained from the original HK model.

A major limitation of the original HK method is that it does not account for monolayer formation and film growth in mesopores prior to the capillary condensation transition (see Fig. 12). The model isotherm given by the original HK model is essentially a step-function isotherm in which the pore is either completely empty (if the pressure is below the pore condensation pressure) or completely filled (if $P > P_c$). The wetting of mesopore surfaces can constitute a substantial contribution to the overall experimental isotherm at low pressures, and hence models that omit such contributions will generate erroneous PSD results. To remedy this deficiency, a two-stage HK adsorption model [114] has been proposed in which the capillary condensation step in the mesopore isotherm is preceded by a step that corresponds to the formation of a monolayer on the pore surface, as shown in Fig. 15b. The two-stage HK model provides a better fit than the original HK model to experimental isotherm data for mesoporous adsorbents.

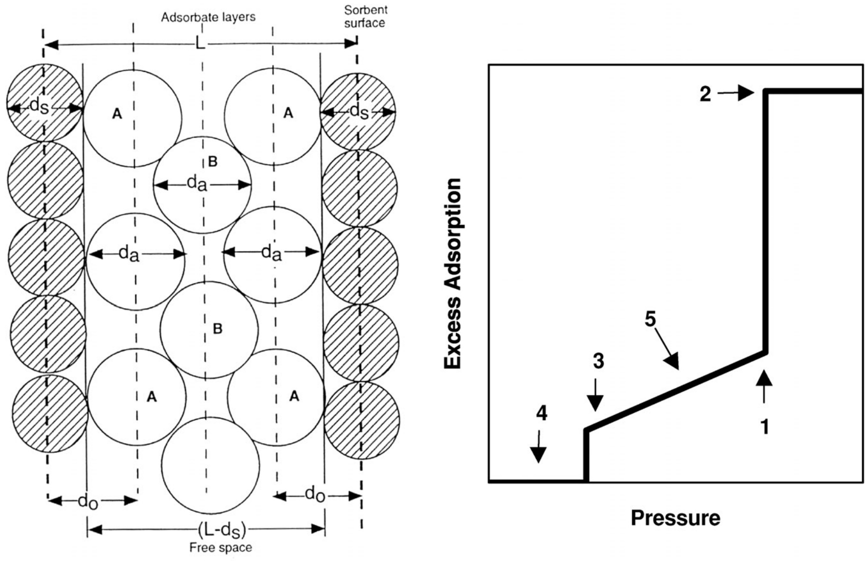

(a) *(b)*

FIG. 15. Illustrations of modified HK adsorption models. (a) Geometric representation slit pore filled with adsorbate [110]. (b) Two-stage HK mesopore isotherm model [114] in which capillary condensation (1) to the filled state (2) is preceded by a wetting transition (3) from an empty state (4) to an intermediate condition characterized by film growth on the pore walls (5). (Reproduced with permission from S. Ramalingam, E. S. Aydil, and D. Maroudas. Molecular dynamics study of the interactions of small thermal and energetic silicon clusters with crystalline and amorphous silicon surfaces. *Journal of Vacuum Science and Technology B,* 2000;19:634–644. Copyright © 2001, AVS.)

3. Dubinin Adsorption Models

In the Dubinin–Radushkevitch (DR) equation [115], an adsorption model derived from a concept of Dubinin [20] based on Polanyi potential theory, the fluid volume V adsorbed in micropores at pressure P is represented empirically as

$$V/V_0 = \exp\{-[RT\ln(P_0/P)]^2/(\beta E_0)^2\} = \exp[-(A/E)^2], \qquad (38)$$

where V_0 is the micropore volume, and E_0 and β are characteristic parameters of the adsorbent surface energy and the adsorbate affinity, respectively. A plot of $\ln(V)$ vs $\ln^2(P_0/P)$ is thus expected to yield a linear relationship. This has been found to be the case over a wide range of relative pressures for some microporous carbons [116], but for many other adsorbents the linear DR relationship does not hold [1]. If a linear plot is obtained, the micropore volume can be determined from the intercept at $P = P_0$.

Dubinin and Astakhov [117] put forward a more general form of Eq. (38), termed the DA equation, in which the square exponent is replaced with an empirical constant with a value between 2 and 6. No physical basis was identified, however, for selecting the value of the exponent. To cast the DR equation into a form more suitable for PSD analysis of heterogeneous microporous solids, Stoeckli [118] suggested an integral form of Eq. (38) involving a structure distribution function $J(B)$ for the micropore PSD,

$$V/V_0 = \int_0^\infty \exp[-B(A/\beta)^2] J(B) dB. \tag{39}$$

In the Dubinin–Stoeckli (DS) method, a Gaussian pore size distribution is assumed for $J(B)$ in Eq. (39), based on the premise that for heterogeneous carbons, the original DR equation holds only for those carbons that have a narrow distribution of micropore sizes. This assumption enables Eq. (39) to be integrated into an analytical form involving the error function [119] that relates the structure parameter B to the relative pressure $A = -RT \ln(P/P_0)$. The structure parameter B is proportional to the square of the pore half-width, for carbon adsorbents that have slit-shaped micropores.

In recent work along similar lines [120], the DS approach was used to calculate PSDs for a set of activated carbons, with a Γ distribution function used to represent the PSD in Eq. (39). The activated carbons were subjected to different activation times, so that the microporosity was more fully developed in the samples with longer activation periods. The pore size results obtained from the DS, HK, and DFT methods were compared. It was found that the HK and DFT methods correctly predicted an increase in the micropore PSD for samples prepared with longer activation times, whereas the DS method did not predict this trend correctly. In another evaluation of the adsorption models, a mock isotherm was generated via GCMC simulation for a hypothetical graphitic carbon with a Gaussian pore size distribution (Fig. 16). The DS, HK, and DFT models were then applied to this hypothetical isotherm to see if the original PSD could be recovered. In general, the shape of the original Gaussian PSD was not reproduced by any of the analysis routines. However, the large amount of "noise" in the unregularized DFT pore size distributions in Fig. 16 strongly suggests that experimental errors have been transmitted into these PSD results and that additional smoothing constraints are needed to interpret the experimental data properly. The DFT model did perform the best in recovering the PSD maxima for hypothetical Gaussian distributions that were centered in the micropore range [120].

Dubinin adsorption models have been used to calculate carbon micropore distributions from experimental isotherm measurements of a number of adsorbates, including nitrogen [120–122], carbon dioxide [122, 123], methane [123], and several other organic molecules [124]. It is has generally been

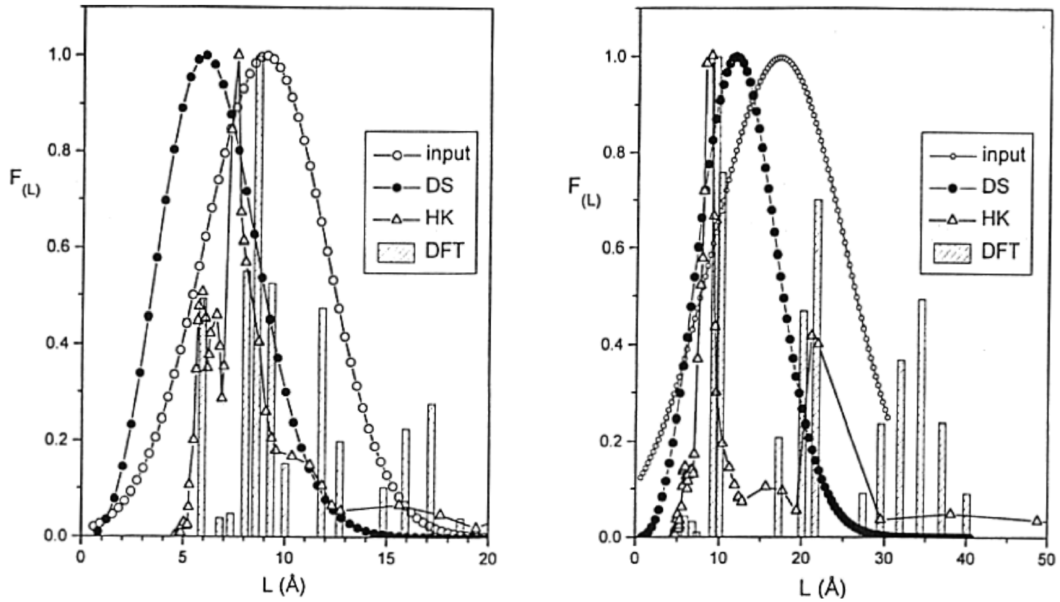

FIG. 16. Comparison of PSDs obtained using the Dubinin–Stoeckli (DS), Horvath–Kawazoe (HK), and density functional theory (DFT) methods to interpret an isotherm generated from molecular simulation of nitrogen adsorption in a model carbon that has a Gaussian distribution of slit pore widths [120]. Results are shown for mean pore widths of 8.9 Å (left) and 16.9 Å (right).

observed that the Dubinin-class adsorption models have a tendency to overconstrain the shape of the PSD, so that the true PSD function is not obtained in many cases. Also, the values of the empirical parameters E_0 and β that appear in the DR and DS equations vary according to the adsorbent–adsorbate pair, but a consistent method for selecting the parameters has not been reported.

D. Classical Adsorption Models

The classical model for describing adsorption in simple geometric pores is based on the Kelvin equation [125], which is derived from the condition of mechanical equilibrium for a curved interface between coexisting vapor and liquid phases in a pore. If the adsorbed liquid completely wets the pore walls, as shown in Fig. 17a, and the vapor phase is assumed to be an ideal gas, then mechanical equilibrium requires that

$$\ln(P_c/P_0) = -2\gamma_l/RT\rho_l(r_k - t), \tag{40}$$

where γ_l is the surface tension, ρ_l is the liquid density, and t is the equilibrium thickness of the film adsorbed on the pore wall. Equation (40) is actually a modified Kelvin (MK) equation in which the pore radius, r_p, is calculated as the sum of the core radius of the vapor–liquid interface, r_k, and the adsorbed film thickness t. The latter quantity is obtained from an

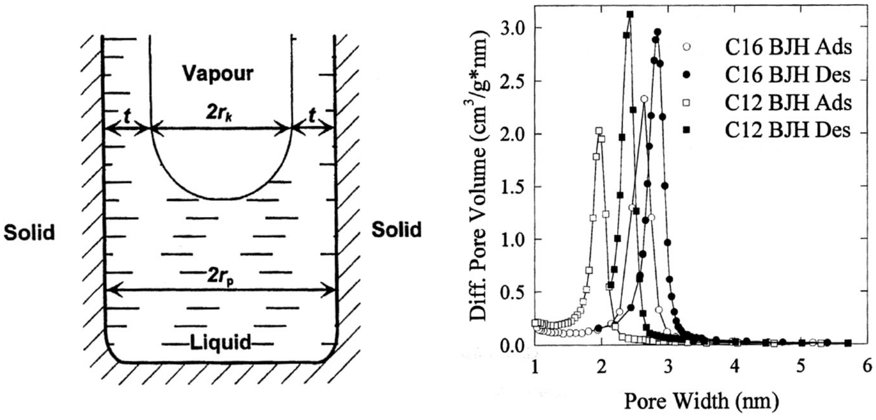

(a) *(b)*

FIG. 17. (a) Schematic of vapor–liquid equilibrium in a wetted pore used in the Kelvin equation model [2]. (b) Comparison of PSD results obtained using the BJH Kelvin equation model to interpret the PSDs of two mesoporous MCM-41 structures, C16 (circles) and C12 (squares) [130]. The open and filled symbols denote PSD results obtained from the adsorption and desorption branches of the isotherm, respectively.

experimental isotherm measured upon a nonporous substrate of the same material as the porous solid [126]. The analytic form of the MK equation can be applied to PSD analysis of mesoporous solids; various prescriptions have been suggested for interpreting the experimental isotherm using this model [28, 127, 128]. For mesoporous materials that exhibit adsorption/desorption hysteresis, the PSD that is obtained will depend on whether the adsorption or desorption branch of the experimental isotherm is selected for the PSD analysis. For capillary condensation in cylindrical pores, the meniscus of the adsorbate is usually assumed to be cylindrical in shape during adsorption but hemispherical during desorption [129]. This results in forms of Eq. (40) for adsorption and desorption that differ by a factor of two on the right-hand side. In general, smaller mean pore sizes are obtained when the adsorption branch is used to interpret the PSD rather than the desorption branch, as shown in Fig. 17b [130] for the PSDs of two MCM-41 samples calculated using the Barrett–Joyner–Halenda (BJH) method [28], the most popular Kelvin-based analysis method.

It has been known for about two decades that the classical Kelvin and MK equation methods underestimate the mean pore sizes of adsorbents that have pores smaller than 75 Å [131, 132]. The error becomes very large for microporous adsorbents, as shown in Fig. 11 [11]. The continuum description of a vapor–liquid interface in a filled capillary breaks down for micropores, in which the adsorbed fluid has a coarse-grained structure and the construct of the surface tension cannot be applied. Also, the Kelvin equation altogether neglects interactions between adsorbate molecules and the pore surface, a significant omission since these interactions are greatly enhanced in micropores. Various studies have established that traditional Kelvin-based adsorption models consistently underestimate the mean pore sizes and PSD maxima of microporous solids. Figure 18, for example, demonstrates that the mean pore sizes obtained for model controlled pore glasses (see Fig. 1) using the BJH method [28] are found to be approximately 1 nm smaller [25] than the pore sizes obtained from the exact geometric calculation as noted in Fig. 2.

The shortcomings of the classical Kelvin-based adsorption models have spurred efforts to modify the Kelvin equation method further so that it may be applied to the characterization of microporous adsorbents. In recent studies of MCM-41 adsorbents [129, 133, 134], it was noted that the MK pore filling correlation can be brought into close agreement with experimental measurements of capillary condensation (Fig. 19) by subtracting a constant value from the $(r_k - t)$ term on the right-hand side of Eq. (40). The value of the adjustment factor was found to be 0.3 nm for nitrogen adsorption at 77 K [129] and 0.438 nm for argon adsorption at 87 K in MCM-41 samples [134]. Although the corrections reproduce the experimental pore filling pressures

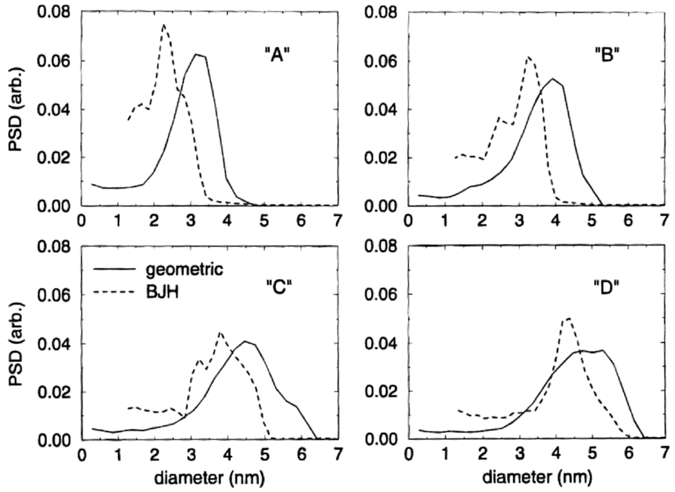

FIG. 18. PSDs for model porous silica glasses [25]. A, B, C, and D are sample glasses prepared by quench MD; the samples differ in mean pore size and porosity. The solid curves are exact geometric PSD results for the model adsorbents; the dashed lines are the PSDs predicted from BJH pore size analysis of simulated nitrogen isotherms for the model porous glasses.

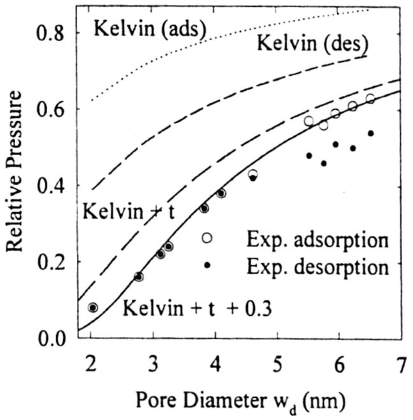

FIG. 19. Comparison of pore filling correlations developed to interpret experimental measurements of the nitrogen condensation pressure at 77 K in MCM-41 samples that have different pore diameters [129]. The dotted and short-dashed lines denote the results for the original Kelvin equation, i.e., $t = 0$ in Eq. (40), with a cylindrical and hemispherical meniscus assumed respectively for the adsorption and desorption cases. The long-dashed line shows the pore filling correlation for the MK model of Eq. (40), and the solid line shows the result when the pore width is adjusted by an additional factor of 0.3 nm.

of MCM-41 materials with reasonable accuracy, no physical justification has been put forth to rationalize this modified form of the Kelvin equation. Consequently, there is no a priori method to predict the correction factor needed for other probe gases and other temperatures, nor is it known whether the empirical correlation will hold for materials other than MCM-41.

Another pore filling model based upon capillary equilibrium in cylindrical pores has recently been proposed in which the condition of thermodynamic equilibrium is modified to include the effects of surface layering and adsorbate–adsorbent interactions [135–137]. Assuming that the vapor–liquid interface is represented by a cylindrical meniscus during adsorption and by a hemispherical meniscus during desorption, and invoking the Defay–Prigogene expression for a curvature-dependent surface tension [21], the equilibrium condition for capillary coexistence in a cylindrical pore is obtained as

$$\begin{aligned}\frac{d(\Delta G)}{dN} = 0 &= \int_{P_\mathrm{g}}^{P_0} \nu_\mathrm{g} dP + \widetilde{\phi}(t, R) - \frac{\nu_\mathrm{l}\gamma_\infty(R-t)}{(R-t-\lambda/2)^2} \\ &= \int_{P_\mathrm{g}}^{P_0} \nu_\mathrm{g} dP + \widetilde{\phi}(R, R) - \frac{2\nu_\mathrm{l}\gamma_\infty(R-t)^2}{[(R-t)(R-t-\lambda)+\lambda\sigma_\mathrm{ff}/4]\,(R-t-\lambda)},\end{aligned} \tag{41}$$

where $d(\Delta G)/dN$ is the Gibbs free energy change per mole adsorbed, ν_g and ν_l are the respective gas and liquid molar volumes at the saturation pressure P_0, γ is the surface tension of the vapor–condensate interface, σ_ff is the adsorbate molecular diameter, R is the pore radius, and $\lambda = (\frac{2}{3})^{1/2}\sigma_\mathrm{ff}$ [135]. The potential field $\widetilde{\phi}(r, R)$ represents the net interaction of an adsorbate molecule at radial coordinate r with the surrounding condensate and solid. This field is given as the difference between the adsorbate–adsorbent and the adsorbate–adsorbate potentials, and it is represented using the 9–3 potential for an adsorbate confined within a cylindrical pore of a structureless Lennard–Jones solid. The adsorbed layer thickness t can be determined for a given pore radius and potential field by solving the equality given by Eq. (41). The capillary coexistence curve can then be constructed by calculating the condensation pressure P_g from Eq. (41) using the known values of film thickness and pore radius. This method was shown to give good agreement with the capillary coexistence curve and pore criticality predicted by DFT for adsorption of nitrogen [135–137] and other probe gases [136] on MCM-41 materials. The method also qualitatively predicts some wetting features of the isotherm below the capillary condensation pressure [135, 136].

Another suggested MK method incorporates an improved model of the statistical adsorbed film thickness into Eq. (40) [138, 139]. In this approach,

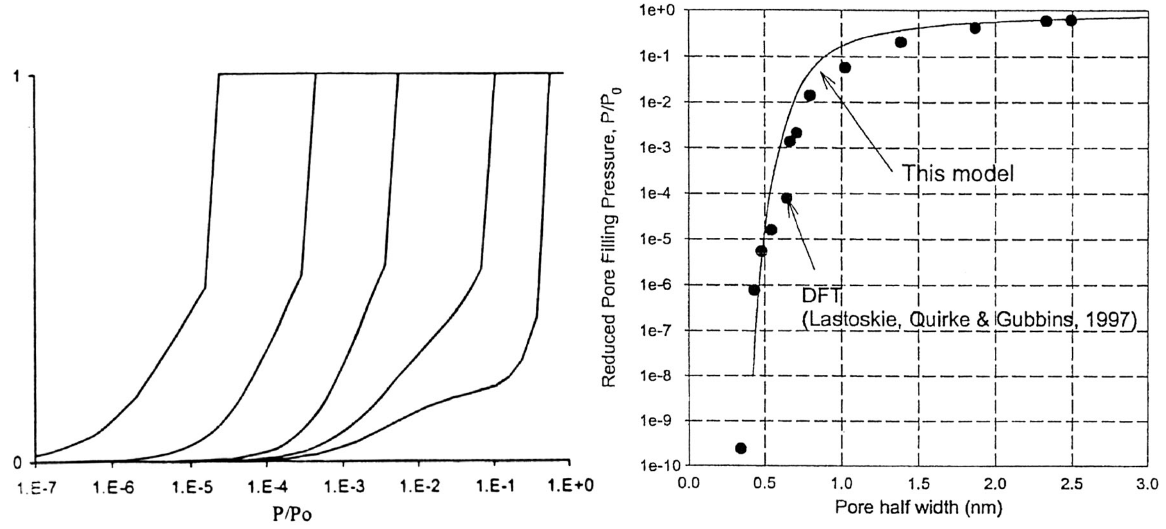

(a) *(b)*

FIG. 20. (a) Model nitrogen adsorption isotherms at 77 K calculated using a modified Kelvin-BET method for carbon slit pores of physical width (reading from left to right) 10.0, 11.4, 14.3, 21.4 and 42.9 Å [138]. (b) Comparison of pore filling pressure correlations for DFT (points) and the MK-BET method (line) for nitrogen adsorption in carbon slit pores at 77 K [139].

the film thickness t is calculated using a modified BET equation to account for molecular layering in pores of finite dimension, with the BET shape parameter calculated from the heat of adsorption of the adsorbate molecule in the micropore. The modified BET equation is also used to represent the amount adsorbed below the capillary condensation pressure, as shown in the model isotherms in Fig. 20a. The MK-BET method is computationally efficient, and as shown in Fig. 20b, it yields a nitrogen pore filling correlation that is in good agreement with DFT results [138, 139]. The MK-BET method assumes that the surface tension and molar volume of the confined fluid do not depend on the pore size. Although there is no physical justification in support of this assumption, the empirical combination of Eq. (40) with a modified BET model for the film thickness gives a surprisingly accurate pore filling correlation for the case of subcritical nitrogen adsorption in slit-shaped carbon pores.

IV. Conclusions

At the present time, the pore filling models that are most frequently used to interpret pore structure from gas adsorption measurements are those based upon simple geometric pore models: density functional theory, the Horvath–Kawazoe method, and variations of the Kelvin equation. It should be recognized that these models are all limited by similar assumptions regarding the pore shape, the chemical homogeneity of the adsorbent surface, and the neglect of pore connectivity. Among the computationally efficient adsorption models that assume a simple pore geometry, DFT is the best model for the determination of the adsorbent pore size distribution [140]. Validation against molecular simulation results has established that DFT provides a realistic model of pore filling for chemically homogeneous porous solids that have simple pore geometries. Molecular simulation methods such as GCMC and GEMC can also be directly employed in simple geometric pore models for PSD characterization, but the molecular simulation approach is considerably more computer-intensive than the analytic pore filling models (i.e., HK, Kelvin equation) or DFT.

DFT and molecular simulation adsorption models give good results over a wide range of temperatures, both subcritical and supercritical, and over the full range of pressures sampled in the experimental adsorption isotherm. The DFT and molecular simulation methods may be used for PSD analysis in both the micropore and the mesopore size range. In contrast, the Kelvin and HK pore filling models are computationally convenient but are more limited in their range of application, although recent modifications of these methods have significantly extended their capabilities. For microporous solids, it is particularly important that the adsorption model includes the effects of gas–solid interactions in the calculation of the theoretical isotherms. This is best accomplished using DFT or a molecular simulation technique.

The accuracy and realism of the pore filling model are the principal consideration in obtaining the correct PSD from inversion of Eq. (14). It should be noted, however, that experimental and numerical considerations also factor into the range and accuracy of the calculated PSD results. Using commercially available gas porosimeters, for example, one can measure the experimental isotherm of the adsorbent to a minimum pressure of approximately 10^{-6} atm. For microporous carbon adsorbents with slit-shaped pores, theoretical results indicate that nitrogen condensation at 77 K occurs at pressures below 10^{-6} atm in pores narrower than 9 Å (Fig. 11). Thus, conventional nitrogen porosimetry cannot access the ultramicropore size distribution and the PSDs of materials such as molecular sieve carbons must be determined by other methods, e.g., size exclusion porosimetry. Another potential source of uncertainty in the PSD result, as noted in Section III, is the extent to which regularization is applied for the inversion of the ill-posed integral of Eq. (14). There is presently no consensus on the form of the regularization constraint that should be used in obtaining the PSD, nor is there an established procedure for selecting the proper value of the smoothing parameter that appears in the objective function. It is important to recognize that regularization can have a profound effect on the shape of the computed pore size distribution and that highly dissimilar PSD results can be obtained from the same experimental isotherm and the same theoretical adsorption model if different regularization techniques are applied.

Although DFT is computationally more efficient than molecular simulation for simple geometric pore models, molecular simulation methods will become progressively more desirable for carrying out pore structure analysis as computer hardware capabilities steadily improve. Molecular simulation has the advantage that it can be readily applied to more complicated adsorbate molecules, and particularly to more complex pore topologies such as the disordered porous model structures described in Section II. This is not the case for DFT. The use of molecular simulation is particularly attractive for developing realistic disordered model porous structures by mimicking the processing of adsorbent materials, as discussed in Section II.A for quench MD simulation of controlled pore glasses. This simulation method has the advantage that it gives a unique pore structure. However, a different simulation approach is required for each new class of materials. Another application of molecular simulation that shows great promise is to use reverse Monte Carlo sampling to generate model amorphous microstructures that are in statistical agreement with adsorbent structural data obtained from scattering experiments. The RMC method described for microporous carbons in Section II.B can be applied to other types of materials, but in general it does not yield a unique structure for the porous solid. How important this feature of nonuniqueness is for pore structure characterization and for prediction of adsorption properties remains to be determined.

It may be possible to alleviate the nonuniqueness problem by using more than one experimental probe technique in the pore structure analysis. Some preliminary work (e.g., Fig. 14) has shown that structure factor measurements from X-ray or neutron diffraction can be effectively combined with sorption porosimetry and/or adsorption calorimetry measurements to characterize semiamorphous porous solids. Sophisticated molecular modeling methods for disordered porous solids are still in an early stage of development and are highly computer-intensive. However, with further improvements in both computing speeds and modeling algorithms, a new set of powerful simulation-based characterization methods for amorphous materials may be expected in the next decade. These simulated model structures offer the tangible prospect of incorporating important features such as pore connectivity, pore shape variations, and surface chemical heterogeneity directly into the adsorbent characterization procedure.

ACKNOWLEDGMENTS

We thank the National Science Foundation (Grant CTS-9733086) and the Department of Energy (Grant DE-FG02-98ER14847) for support of this research.

REFERENCES

1. S. J. Gregg and K. S. W. Sing, *Adsorption, Surface Area and Porosity,* Academic Press, London, 1982, p. 37.
2. F. Rouquerol, J. Rouquerol, and K. Sing, *Adsorption by Powders and Porous Solids,* Academic Press, London, 1999, p. 227.
3. C. G. Salazar, A. Sepulveda-Escribano, and F. Rodriguez-Reinoso, *Stud. Surf. Sci. Catal.* **128,** 303 (2000).
4. A. Albiniak, E. Broniek, M. Jasienko-Halat, A. Jankowska, J. Kaczmarczyk, T. Siemieniewska, R. Manso, and J. A. Pajares, *Stud. Surf. Sci. Catal.* **128,** 653 (2000).
5. T. Goworek, B. Jasinska, J. Wawryszczuk, K. Ciesielski, and J. Goworek, *Stud. Surf. Sci. Catal.* **128,** 557 (2000).
6. H. Kanda, M. Miyahara, T. Yoshioka, and M. Okazaki, *Langmuir* **16,** 6622 (2000).

7. M. Kruk, M. Jaroniec, Y. Sakamoto, O. Terasaki, R. Ryoo, and C. H. Ko, *J. Phys. Chem. B* **104,** 292 (2000).
8. A. V. Neimark, P. I. Ravikovitch, M. Grun, F. Schuth, and K. K. Unger, *J. Colloid Interface Sci.* **207,** 159 (1998).
9. J. D. F. Ramsay, S. Kallus, and E. Hoinkis, *Stud. Surf. Sci. Catal.* **128,** 439 (2000).
10. E. I. Segarra and E. D. Glandt, *Chem. Eng. Sci.* **49,** 2953 (1994).
11. C. M. Lastoskie, N. Quirke, and K. E. Gubbins, *Stud. Surf. Sci. Catal.* **104,** 745 (1997).
12. D. Nicholson and N. G. Parsonage, *Computer Simulation and the Statistical Mechanics of Adsorption,* Academic Press, London, 1982.
13. A. Z. Panagiotopoulos, *Mol. Phys.* **62,** 701 (1987).
14. R. L. McGreevy and L. Putszai, *Mol. Simul.* **1,** 359 (1988).
15. C. M. Lastoskie, K. E. Gubbins, and N. Quirke, *J. Phys. Chem.* **97,** 4786 (1993).
16. P. I. Ravikovitch, G. L. Haller, and A. V. Neimark, *Stud. Surf. Sci. Catal.* **117,** 77 (1998).
17. W. G. Madden and E. D. Glandt, *J. Stat. Phys.* **51,** 537 (1988).
18. L. Zhang and P. R. Van Tassel, *J. Chem. Phys.* **112,** 3006 (2000).
19. G. Horvath and K. Kawazoe, *J. Chem. Eng. Japan* **16,** 474 (1983).
20. M. M. Dubinin and L. V. Radushkevich, *Proc. Acad. Sci. USSR* **55,** 331 (1947).
21. R. Defay and I. Prigogine, *Surface Tension and Adsorption,* Longmans, Green, Bristol, 1966.
22. C. M. Lastoskie, K. E. Gubbins, and N. Quirke, *Langmuir* **9,** 2693 (1993).
23. G. M. Davies, N. A. Seaton, and V. S. Vassiliadis, *Langmuir* **15,** 8235 (1999).
24. L. D. Gelb and K. E. Gubbins, *Langmuir* **14,** 2097 (1998).
25. L. D. Gelb and K. E. Gubbins, *Langmuir* **15,** 305 (1999).
26. W. Haller, *Nature* **206,** 693 (1965).
27. P. Levitz, G. Ehret, S. K. Sinha, and J. M. Drake, *J. Chem. Phys.* **95,** 6151 (1991).
28. E. P. Barrett, L. G. Joyner, and P. P. Halenda, *J. Am. Chem. Soc.* **73,** 373 (1951).
29. P. Pfeifer, G. P. Johnston, R. Deshpande, D. M. Smith, and A. J. Hurd, *Langmuir* **7,** 2833 (1991).
30. P. Levitz, *Adv. Colloid Interface Sci.* **76,** 71 (1998).
31. R. J. M. Pellenq, A. Delville, H. van Damme, and P. Levitz, *Stud. Surf. Sci. Catal.* **128,** 1 (2000).
32. K. T. Thomson and K. E. Gubbins, *Langmuir* **16,** 5761 (2000).
33. B. E. Warren, *X-Ray Diffraction,* Dover, New York, 1990, p. 116.
34. N. Metropolis and S. Ulam, *J. Am. Stat. Assoc.* **44,** 335 (1949).
35. B. McEnaney, *Carbon* **26,** 267 (1988).
36. H. March and P. L. Walker, Jr., in *Chemistry and Physics of Carbon,* Marcel Dekker, New York, 1979, Vol. 15, Chap. 3.
37. B. McEnaney, T. J. Mays, and X. Chen, *Fuel* **77,** 557 (1998).
38. J. Rodriguez, F. Ruette, and J. Laine, *Carbon* **32,** 1536 (1994).
39. J. R. Dahn, W. Xing, and Y. Gao, *Carbon* **35,** 825 (1997).
40. N. A. Seaton, S. P. Friedman, J. M. D. MacElroy, and B. J. Murphy, *Langmuir* **13,** 1199 (1997).
41. M. P. Allen and D. J. Tildesley, *Computer Simulaton of Liquids,* Clarendon Press, Oxford, 1987.
42. K. S. Page and P. A. Monson, *Phys. Rev. E* **54,** R29 (1996).
43. K. S. Page and P. A. Monson, *Phys. Rev. E* **54,** 6557 (1996).
44. L. Sarkisov and P. A. Monson, *Stud. Surf. Sci. Catal.* **128,** 21 (2000).
45. J. K. Johnson, J. A. Zollweg, and K. E. Gubbins, *Mol. Phys.* **78,** 591 (1993).
46. R. D. Kaminsky and P. A. Monson, *J. Chem. Phys.* **95,** 2936 (1991).
47. J. M. D. MacElroy and K. Raghavan, *J. Chem. Phys.* **93,** 2068 (1990).

48. K. S. W. Sing, D. H. Everett, R. A. W. Haul, L. Moscou, R. A. Pierotti, J. Rouquerol, and T. Siemieniewska, *Pure Appl. Chem.* **57,** 603 (1985).
49. M. W. Maddox, C. M. Lastoskie, N. Quirke, and K. E. Gubbins, in *Fundamentals of Adsorption 5* (M. D. LeVan, ed.), Kluwer Academic, Boston, 1996, p. 571.
50. G. S. Heffelfinger and F. van Swol, *J. Chem. Phys.* **100,** 7548 (1994).
51. W. D. Machin and P. D. Golding, *J. Chem. Soc. Faraday Trans.* **86,** 175 (1990).
52. Y. Lu, G. Cao, R. P. Kale, S. Prabakar, G. P. Lopez, and C. J. Brinker, *Chem. Mater.* **11,** 1223 (1999).
53. O. D. Velev, T. A. Jede, R. F. Lobo, and A. M. Lenhoff, *Nature* **389,** 447 (1997).
54. C. T. Kresge, M. E. Leoniwicz, W. J. Roth, J. C. Vartuli, and J. S. Beck, *Nature* **359,** 710 (1992).
55. L. Zhang and P. R. Van Tassel, *Mol. Phys.* **98,** 1521 (2000).
56. P. R. Van Tassel, *J. Chem. Phys.* **107,** 9530 (1997).
57. P. R. Van Tassel, *Phys. Rev. E* **60,** R25 (1999).
58. J. A. Given and G. Stell, *J. Chem. Phys.* **97,** 4573 (1992).
59. M. L. Rosinberg, G. Tarjus, and G. Stell, *J. Chem. Phys.* **100,** 5172 (1994).
60. P. R. Van Tassel, J. Talbot, P. Viot, and G. Tarjus, *Phys. Rev. E* **56,** R1229 (1997).
61. J. K. Percus and G. J. Yevick, *Phys. Rev.* **110,** 1 (1958).
62. J. P. Olivier, in *Fundamentals of Adsorption 6* (F. Meunier, ed.), Elsevier, Paris, 1998, p. 207.
63. W. H. Press, *Numerical Recipes: The Art of Scientific Computing,* Cambridge University Press, New York, 1986.
64. M. v. Szombathely, P. Brauer, and M. Jaroniec, *J. Comput. Chem.* **13,** 17 (1992).
65. W. A. House, *J. Colloid Interface Sci.* **67,** 166 (1978).
66. P. H. Merz, *J. Comp. Phys.* **38,** 64 (1980).
67. C. H. W. Vos and L. K. Koopal, *J. Colloid Interface Sci.* **105,** 183 (1985).
68. G. M. Davies and N. A. Seaton, *Langmuir* **15,** 6263 (1999).
69. G. M. Davies and N. A. Seaton, *Carbon* **36,** 1473 (1998).
70. V. Y. Gusev, J. A. O'Brien, and N. A. Seaton, *Langmuir* **13,** 2815 (1997).
71. S. Samios, A. K. Stubos, N. K. Kanellopoulos, R. F. Cracknell, G. K. Papadopoulos, and D. Nicholson, *Langmuir* **13,** 2795 (1997).
72. A. Vishnyakov, P. Ravikovitch, and A. Neimark, *Langmuir* **15,** 8736 (1999).
73. W. A. Steele, *Surf. Sci.* **36,** 317 (1973).
74. H. Liu, L. Zhang, and N. A. Seaton, *Chem. Eng. Sci.* **47,** 4393 (1992).
75. H. Liu and N. A. Seaton, *Chem. Eng. Sci.* **49,** 1869 (1994).
76. M. Lopez-Ramon, J. Jagiello, T. Bandosz, and N. Seaton, *Langmuir* **13,** 4435 (1997).
77. N. A. Seaton, J. R. P. B. Walton, and N. Quirke, *Carbon* **27,** 853 (1989).
78. P. I. Ravikovitch, G. L. Haller, and A. V. Neimark, *Adv. Colloid Interface Sci.* **76,** 203 (1998).
79. R. Nilson and S. K. Griffiths, *J. Chem. Phys.* **111,** 4281 (1999).
80. R. Evans, in *Inhomogeneous Fluids* (D. Henderson, ed.), Marcel Dekker, New York, 1992, Chap. 5.
81. J. A. Barker and D. Henderson, *J. Chem. Phys.* **47,** 4714 (1967).
82. J. D. Weeks, D. Chandler, and H. C. Andersen, *J. Chem. Phys.* **54,** 5237 (1971).
83. N. F. Carnahan and K. E. Starling, *J. Chem. Phys.* **51,** 635 (1969).
84. Y. Rosenfeld, *Phys. Rev. Lett.* **63,** 980 (1989).
85. E. Kierlik and M. L. Rosinberg, *Phys. Rev. A* **42,** 3382 (1990).
86. P. Tarazona, *Phys. Rev. A* **31,** 2672 (1985).
87. P. Tarazona, *Phys. Rev. A* **32,** 3148 (1985).
88. P. Tarazona, U. Marini Bettolo Marconi, and R. Evans, *Mol. Phys.* **60,** 573 (1987).

89. T. M. Reed and K. E. Gubbins, *Applied Statistical Mechanics,* Butterworth–Heinemann, Stoneham, MA, 1973.
90. R. Dombrowski, D. Hyduke, and C. M. Lastoskie, *Langmuir* **16,** 5041 (2000).
91. J. P. Olivier, *J. Porous Mater.* **2,** 9 (1995).
92. P. Ravikovitch, A. Vishnyakov, R. Russo, and A. Neimark, *Langmuir* **16,** 2311 (2000).
93. A. V. Neimark and P. I. Ravikovitch, *Langmuir* **13,** 5148 (1997).
94. N. Quirke and S. R. R. Tennison, *Carbon* **34,** 1281 (1996).
95. S. Scaife, P. Kluson, and N. Quirke, *J. Phys. Chem. B* **104,** 313 (2000).
96. P. I. Ravikovitch, S. C. O. Domhnaill, A. V. Neimark, F. Schuth, and K. K. Unger, *Langmuir* **11,** 4765 (1995).
97. C. T. Kresge, M. E. Leonowicz, W. J. Roth, J. C. Vartuli, and J. S. Beck, *Nature* **359,** 710 (1992).
98. P. Ravikovitch, D. Wei, W. T. Chueh, G. L. Haller, and A. Neimark, *J. Phys. Chem. B* **101,** 3671 (1997).
99. K. Schumacher, P. I. Ravikovitch, A. Du Chesne, A. Neimark, and K. K. Unger, *Langmuir* **16,** 4648 (2000).
100. C. Y. Chen, S. Q. Xiao, and M. E. Davis, *Micropor. Mater.* **4,** 1 (1995).
101. R. A. Pierotti and H. E. Thomas, *Surf. Colloid Sci.* **4,** 241 (1971).
102. J. Frenkel, *Kinetic Theory of Liquids,* Clarendon Press, Oxford, 1946.
103. G. D. Halsey, *J. Am. Chem. Soc.* **74,** 1082 (1952).
104. T. L. Hill, *J. Chem. Phys.* **17,** 668, (1949).
105. D. H. Everett and J. C. Powl, *J. Chem. Soc. Faraday Trans. 1* **72,** 619 (1976).
106. A. Saito and H. C. Foley, *AIChE J.* **37,** 429 (1991).
107. L. S. Cheng and R. T. Yang, *Chem. Eng. Sci.* **49,** 2599 (1994).
108. L. S. Cheng and R. T. Yang, *Adsorption* **1,** 187 (1995).
109. R. K. Mariwala and H. C. Foley, *Ind. Eng. Chem. Res.* **33,** 2314 (1994).
110. S. U. Rege and R. T. Yang, *AIChE J.* **46,** 734 (2000).
111. R. J. Dombrowski, C. M. Lastoskie, and D. R. Hyduke, *Colloid Surf. A* (2001), in press.
112. A. Muller, *Proc. Roy. Soc. London* **A154,** 624 (1936).
113. C. M. Lastoskie, *Stud. Surf. Sci. Catal.* **128,** 475 (2000).
114. R. J. Dombrowski and C. M. Lastoskie, submitted for publication (2001).
115. M. M. Dubinin, *Chem. Rev.* **60,** 235 (1960).
116. M. M. Dubinin, in *Chemistry and Physics of Carbon* (P. L. Walker, ed.), Marcel Dekker, New York, 1966, p. 51.
117. M. M. Dubinin and V. A. Astakhov, *Adv. Chem. Ser.* **102,** 69 (1970).
118. H. F. Stoeckli, *J. Colloid Interface Sci.* **59,** 184 (1977).
119. R. C. Bansal, J. B. Donnet, and H. F. Stoeckli, *Active Carbon,* Marcel Dekker, New York, 1988.
120. D. L. Valladares, F. Rodriguez-Reinoso, and G. Zgrablich, *Carbon* **36,** 1491 (1998).
121. M. el-Merraoui, M. Aoshima, and K. Kaneko, *Langmuir* **16,** 4300 (2000).
122. D. Cazorla-Amoros, J. Alcaniz-Monge, M. A. de la Casa-Lillo, and A. Linares-Solano, *Langmuir* **14,** 4589 (1998).
123. F. Stoeckli, A. Guillot, D. Hugi-Cleary, and A. M. Slasli, *Carbon* **38,** 938 (2000).
124. M. Domingo-Garcia, I. Fernandez-Morales, F. J. Lopez-Garzon, and C. Moreno-Castilla, *Langmuir* **13,** 1218 (1997).
125. W. T. Thomson, *Phil. Mag.* **42,** 448 (1871).
126. M. Jaroniec, M. Kruk, and J. P. Olivier, *Langmuir* **15,** 5410 (1999).
127. R. W. Cranston and F. A. Inkley, in *Advances in Catalysis,* Vol. 9, Academic Press, New York, 1957, p. 143.
128. D. Dollimore and G. R. Heal, *J. Appl. Chem.* **14,** 109 (1964).

129. M. Kruk, M. Jaroniec, and A. Sayari, *Langmuir* **13,** 6267 (1997).
130. M. Kruk, M. Jaroniec, and A. Sayari, *J. Phys. Chem. B* **101,** 583 (1997).
131. J. R. Fisher and J. N. Israelachvili, *J. Colloid Interfac. Sci.* **80,** 528 (1981).
132. J. P. R. B. Walton and N. Quirke, *Mol. Simul.* **2,** 361 (1989).
133. M. Kruk, M. Jaroniec, J. M. Kim, and A. R. Ryoo, *Langmuir* **15,** 5279 (1999).
134. M. Kruk and M. Jaroniec, *Chem. Mater.* **12,** 222 (2000).
135. C. G. Sonwane and S. K. Bhatia, *Chem. Eng. Sci.* **53,** 3143 (1998).
136. C. G. Sonwane, S. K. Bhatia, and N. Calos, *Ind. Eng. Chem. Res.* **37,** 2271 (1998).
137. S. K. Bhatia and C. G. Sonwane, *Langmuir* **14,** 1521 (1998).
138. C. Nguyen and D. D. Do, *Langmuir* **15,** 3608 (1999).
139. D. D. Do, C. Nguyen, and H. D. Do, *Colloid Surf. A* in press, (2001).
140. C. M. Lastoskie and K. E. Gubbins, *Stud. Surf. Sci. Catal.* **128,** 41 (2000).